Enhanced Biomechanical Performance of Additively Manufactured Ti-6Al-4V Bone Plates

Saurabh Kumar Gupta[1], Nagur Shahidsha[1], Sumit Bahl[1,#], Dhaval Kedaria[1], Sarat Singamneni[2], Prasad K.D.V. Yarlagadda[3], Satyam Suwas[1], Kaushik Chatterjee[1*]

[1]Department of Materials Engineering, Indian Institute of Science, Bangalore, India

[2]Department of Mechanical Engineering, Auckland University of Technology, Auckland, New Zealand

[3]School of Chemistry, Physics and Mechanical Engineering, Science and Engineering Faculty, Queensland University of Technology, Brisbane, Australia

*****_Author to whom all correspondence should be addressed:_

kchatterjee@iisc.ac.in; +91-80-22933408

[#]Current address: Oak Ridge National Laboratory, Oak Ridge, TN, USA

Abstract

As the global trauma fixation devices market expands rapidly, it is imperative to improve the production of fixation devices through enhanced design accuracy and fit for best performance and maximum patient comfort. Selective laser melting (SLM) is one of the mature additive manufacturing methods, which provides a viable route for the rapid production of such devices. In this work, the ability of SLM to produce near-net-shape parts, as desired for medical implants, was utilized for the fabrication of bone plates from Ti-6Al-4V alloy powder. Martensitic microstructure obtained after printing of alloy resulted in poor ductility, limiting its application in the field of orthopedics. A specially designed repeated cyclic heating and cooling close to but below the β-transus was used to transform to a bimodal microstructure without the need for plastic deformation prior to heat treatment for improving the ductility. Bone plates subjected to this heat treatment were mechanically tested by means of tensile and 3-point bend tests and demonstrated large improvement in ductility, and the values were comparable to those similar plates prepared from wrought alloy. Other important properties required for implants such as corrosion resistance in simulated body fluid and cytocompatibility *in vitro* assessed using MC3T3-E1 bone were studied. These results for the bone plate after heat treatment were excellent and similar to those of the additively manufactured and wrought plates. Taken together, the performance of the additively manufactured bone plates after subjecting to heat treatment was similar to those of bone plate manufactured using wrought alloy. These results have important implications for the fabrication of patient-specific metallic orthopedic devices using SLM without compromising their biomechanical performance by subjecting them to a tailored heat treatment.

Keyword: Bone plate; Ti-6Al-4V alloy; Selective laser melting; Microstructure; Mechanical properties; Heat treatment

1. Introduction

The global trauma fixation devices market was valued at $11.71 billion in 2016 and is expected to reach $16.65 billion in 2021 (*Global Trauma Fixation Devices Market 2017-2021*, 2017) Revision surgeries for hip and knee are also expected to increase by 137% and 607%, respectively, between the years 2005 and 2030 (Kurtz et al., 2007). As the market expands rapidly, it is imperative to improve the production of fixation devices through enhanced design accuracy and fit for best performance and maximum patient comfort.

Medical devices are currently prepared by conventional techniques of formative and subtractive manufacturing. These techniques yield implants of standardized geometry and are not customized to meet patient-specific needs for the best anatomical fit. Moreover, some implant designs involve complex geometries, which are difficult to realize accurately through conventional fabrication techniques. Premature implant failure is a serious challenge in the biomedical industry that compromises patient health and adds significantly to healthcare costs. Poor adaptability of the implant to the anatomy of individual patients is a major cause of failure (Didier et al., 2017).

Bone plates prepared by processing routes such as forging and casting, etc., often adapt poorly to the patient's anatomy and can lead to inadequate healing, aside from the risk of implant failure. During implantation, the surgeon must shape the implant gradually by successive plastic deformations (bending and twisting) to map the contour of the patient's bone. Nevertheless, the fit is still not ideal. Consequently, the surgeon must screw the implant to the bone to force it to adapt to the bone morphology. Once screwed, it generates undesirable stresses even in the absence of any loads (Didier et al., 2017). The resultant stresses are detrimental to the implant's life. Several strategies have been proposed for the optimal fitting of the implant (Harith et al., 2016, 2014).

The 3D printing technologies that were used mostly for rapid prototyping have gradually evolved and emerged as the additive manufacturing solutions offering promising solutions in different application areas, in particular, for medical devices such as bone-fixation devices, based on the freedom to make more complex shapes (Frazier, 2014; Liu and Shin, 2019; Ngo et al., 2018). While there are about half a dozen successful techniques in additive manufacturing, selective laser melting (SLM) scores high when it comes to manufacturing complex medical implants and devices in metals. As with the other additive technologies, SLM is a layer by layer fabrication method, which can build 3D parts from a powder bed using a laser with the aid of computer-aided design (CAD) models. SLM is now well established for the popular metallic biomaterials such as stainless steels, titanium alloys, and Co-Cr alloys that are used for load-bearing applications, including total hip/ knee replacements, spinal prosthesis, and dental implants, etc. Titanium and its alloys, specifically commercially-pure Ti (cp-Ti) and Ti-6Al-4V, are the most desirable biomaterials for several of these implants owing to their excellent biocompatibility, high corrosion resistance, low density, low mismatch of elastic modulus with bone, and high specific strength (Fang et al., 2018; Geetha et al., 2009). With the advancements in clinical imaging techniques and design software, patient-specific bone fixation plates can be designed after scanning the defect site by magnetic resonance imaging (MRI) or X-ray microcomputed tomography and 3D virtual reconstruction. When combined with AM, this strategy can lead to the rapid production of patient-specific bone plates that offer more comfort during and after surgery than conventional plates.

Despite its promise, various studies have revealed that processing by the SLM process may result in limitations in the printed parts such as porosity, undesired non-equilibrium microstructure, and high residual tensile stresses, etc. which can compromise the performance of the built parts. Optimizing SLM process parameters such as laser scan speed, laser power, hatch spacing, and powder layer thickness, etc. and the use of defect-free powder particles for

printing can mitigate some of the limitations in the printed parts (Ali et al., 2018; Fan and Feng, 2018; Yang et al., 2016).

Studies have confirmed that rapid solidification during SLM of Ti-6Al-4V alloy results in martensitic microstructure, and consequently, the additively manufactured parts show poor ductility (Vrancken et al., 2012; Wu et al., 2016). Thus, an as-prepared SLM Ti-6Al-4V bone plate is prone to mechanical failure either during surgery for minor deformation or while the bone plates are in service due to biomechanical loads. Thus, whereas SLM offers near-net-shape manufacturing of personalized implants, their clinical use is limited by their poor mechanical performance.

Several groups tried to improve the ductility of the additively manufactured parts by hot isostatic pressing (HIP), heat treatment, or their combination (Ter Haar and Becker, 2018; Vrancken et al., 2012). HIP improves mechanical properties by collapsing the voids and reducing the number of defects in the as-manufactured material (Qiu et al., 2013a). In a different strategy, one research group altered the process parameters for fabricating components while maintaining the same relative density of components and showed that ductility could be improved by controlling the volume fraction of α and α′ phases in the material (Liu et al., 2019a). A higher volume fraction of the highly strained α′ lowers the ductility of titanium. However, the resultant ductility in these studies did not match that of the wrought alloy. In the field of titanium metallurgy, it is widely accepted that the bimodal microstructure imparts good mechanical properties such as high ductility and good strength. In recent work, our group proposed a novel heat treatment schedule for SLM Ti-6Al-4V involving repeated cyclic heating and cooling below the β-transus to generate the bimodal microstructure that resulted in excellent tensile ductility and toughness with minimal loss in tensile strength (Sabban et al., 2019).

The aim of this work was to apply the heat treatment schedule to bone plates fabricated by AM of Ti-6Al-4V for enhancing the biomechanical performance of the plates. Model bone plates of Ti-6Al-4V were designed and fabricated by SLM for osteosynthesis, and subsequently, subjected to the cyclic thermal treatment. We assessed the microstructure, porosity, hardness, electrochemical, tensile properties, and *in-vitro* cytocompatibility of the as-manufactured and heat-treated plates by extracting sample coupons from the bone plates. The performance of the whole plate was assessed using a combination of 3-point bend tests and was compared with bone plates of the same design fabricated by machining of wrought Ti-6Al-4V.

2. Materials and methods

2.1 Design and fabrication of bone plates

Ti-6Al-4V bone plates were printed using the Renishaw AM400 laser melting system at the Auckland University of Technology, New Zealand with the processing parameters as listed in Table 1. Alloy powder of the following composition was used for fabricating the bone plates: 6.00 ± 0.50% Al, 4.00 ± 0.50% V, Fe ≤ 0.25, O ≤ 0.13, C ≤ 0.08, N ≤ 0.05, H ≤ 0.012, and balance Ti (by mass). In one fabrication schedule, a total of five plates were built of the following dimensions: 70 mm length, 17.5 mm width with the holes (for fitting screws) of radius 2.8 mm, and thickness 3 mm. The schematic design of the plate is shown in Figure 1. Z-axis is considered as the build direction throughout this study. Bone plates were stacked in two columns of five plates each on the build plate. The surfaces of the bone plates were covered with support structures for easy separation after fabrication. Post-fabrication, plates were subjected to heat treatment in a furnace filled with Argon gas for stress relief. The temperature was increased to 730 °C over 1 h and then held for 2 h. The furnace was powered off, and the furnace door was opened when the temperature dropped below 400 °C. Subsequently, wire-EDM (electro-discharge machining) was used to separate plates from the stacks. The surface

finishing of the bone plates was done by milling to obtain a smooth surface. After milling bone plates have thickness of 2.9 mm and surface roughness (Ra) was 1.2 ± 0.4 µm. Energy density is calculated using the formula given by:

$$\boldsymbol{E = \frac{P}{v*h*t}} \qquad \textbf{Eq. 1}$$

where P is the laser power [W], v is the scanning speed [mm/s], h is the hatching space [mm]. and t is the layer thickness [mm]. Energy density used here was 89 J/mm^3 and is sufficient for binding the material completely (Kasperovich et al., 2016).

β-transus temperature was obtained from differential scanning calorimetry (DSC). The plates were subjected to a cyclic heat treatment, as shown in Figure S1. All bone plates were individually sealed in vacuum tubes (pressure <10^{-5} mbar) prior to heat treatment in the furnace to avoid oxidation. Hereafter, as-fabricated plates are referred to as AM, whereas the heat-treated bone plates as HT. For comparison with conventionally manufactured parts, bone plates of identical design and dimensions were prepared by machining of wrought Ti-6Al-4V sheets. These plates are referred to as WR, hereafter.

2.2 X-ray microcomputed tomography

Bulk structural defects, such as pores and micro-cracks, in the samples, were characterized using X-ray micro-computed tomography (Xradia Versa XRM500, 10W, 140 kV). A small cylindrical volume of 2.9 mm height and 2.9 mm diameter was scanned. The porosity visualization was done using the AVIZO software. Images were collected at 1.125 voxel size.

2.3 X-ray diffraction and texture analysis

For phase identification, X-ray diffraction (XRD) analysis was performed using Panalytical X'Pert PRO Diffractometer with Cu Kα (λ = 1.54 A°) radiation at 40 kV and 30 mA. Scanning was done in the range of 2θ from 30° to 120° with a step size of 0.033° and a scan speed of

0.0106 °/s. XRD scanning was done on both XY and XZ surface of the AM and HT bone plates (Figure 1). Bulk texture measurement was performed in an X-ray texture goniometer based on Schulz reflection geometry (Rigaku Smartlab XRD) with Cu-Kα source at 45kV and 30 mA on XY surface. All samples were prepared by standard metallographic procedures followed by electropolishing (Struers LectroPol 5) at 40 V in an electrolyte with a composition of 60 ml perchloric acid, 360 ml butoxy ethanol, and 600 ml methanol.

2.4 Microstructural characterization

Samples for optical microscopy, scanning electron microscopy, and electron backscatter diffraction (EBSD) were prepared by standard metallographic procedures followed by electropolishing. Etching of the samples was done in the mixture composed of 92 ml DI water, 6 ml HNO_3 and 2 ml HF to observe microstructure. Microstructural analysis was done using an inverted optical microscope (Carl Zeiss MAT 200 Motorized Axio Vision 4.7.2 version) and a scanning electron microscope (SEM, ESEM Quanta 200 FEI). EBSD with step size of 0.1 and 0.2 µm was done in GeminiSEM 450 equipped with Velocity EBSD detector. To improve indexing in AM sample, additional stress relieving was performed at 300 °C for 2 h.

2.5 Mechanical characterization

Micro-hardness tests were performed using the Vickers micro-hardness tester (Future-Tech FM-800) with 200 gf load and 10 s dwell time. The hardness measurements were done at various locations of the bone plate over the XY and YZ surfaces. Micro-tensile testing was done for the specimens using Instron 5567 screw-driven universal testing machine (UTM) at ambient conditions. Tests were done in displacement control at a strain rate of 10^{-3} s^{-1} for all conditions. The specimens used in this test were cut from two identical portions of the bone plate, as shown in Figure S1a and polished by following standard metallographic procedures. All tensile samples were of 1 mm thickness and the tensile axis was placed perpendicular to the build direction (BD) of the plate. Dimension of micro-tensile specimen is shown in Figure

S1b. Fractography was done on the fractured surface perpendicular to the tensile axis by SEM analysis.

The 3-point bend tests were performed on the intact bone plates using the Instron 8032 servo-hydraulic UTM with a load capacity of 100 kN. The span length (L) and deformation rate used are 45 mm and 0.006 mm/s, respectively. Bone plates were polished, as performed conventionally for metallography, before performing the test.

2.6 Electrochemical characterization

Corrosion behavior of the samples was assessed in a simulated body fluid (SBF) environment at pH 7.4 using an electrochemical analyzer (CHI604E, CH Instruments) with the standard electrode comprising of platinum as the counter electrode and saturated calomel electrode as the reference electrode. SBF composition was prepared as reported (Bahl et al., 2014). All corrosion samples were polished by following standard metallographic techniques followed by electropolishing. Final Test specimens were made by soldering with copper wire followed by mounting using polymer resin. Surface area of 5*5 mm^2 is exposed to SBF. The sample was immersed in SBF for 3 h to stabilize the open circuit potential (OCP). Measurements were performed with the following parameters: initial E = -0.9 V vs SCE, final E = 1.5 V vs SCE, and scan rate = 0.2 mV/s. Corrosion potential (E_{corr}) and current density (I_{corr}) were determined from Tafel plots. Three replicates were studied for statistical significance.

2.7 Cell studies

Cytocompatibility of AM, HT, and WR plates was studied *in vitro* using MC3T3-E1 pre-osteoblasts derived from mouse calvaria. The cells were cultured in α-MEM (minimum essential medium) containing 10 % FBS (fetal bovine serum) and 1% antibiotic (Sigma). Samples of a square cross-section of 4 x 4 mm^2 were cut using EDM for the biological studies. The samples were polished following standard metallographic techniques and then finally

electropolished. The samples were sterilized by immersing in 70 % ethanol for 30 min followed by UV exposure for 30 min at each side.

After sterilization, samples were transferred to individual wells of a 96-well tissue culture polystyrene (TCPS) plate and preconditioned in 300 µL complete culture medium for 18 h. 3.0 x 10^3 cells were seeded in each well containing a sample and incubated at 37 °C with 5 % CO_2. Cell attachment and proliferation were assessed by the Alamar blue assay (Sigma) at days 1, 4 and 7 after seeding. Briefly, at each time point, 10 µL sterile Alamar blue reagent was mixed with 100 µL medium and added to each well. After incubation, the media was transferred to a separate well, and the fluorescence was measured at 530 nm excitation and 590 nm emission using a multi-plate reader (Synergy HT, Biotek). Cell morphology was analyzed at days 1, 4 and 7 after staining F-actin and nucleus. The cells were fixed with 3.7 % formaldehyde for 30 min. Subsequently, cells were permeabilized with 0.2 % Triton X (Sigma) for 15 min at RT. F-actin and the nuclei were stained by 25 µg/mL Alexa Fluor 488 phalloidin (Invitrogen) for 15 min at RT and 1 µg/mL Hoechst, (Sigma) for 7 min, respectively prior to imaging using an epi-fluorescence microscope (Olympus IX-71). statistical analysis of quantitative data of Alamar blue assay was done using Analysis of variance (ANOVA) with Tukey's test. Statistically significant difference was considered at $p < 0.05$.

3. Results

3.1. Characterization of porosity

Porosity is one of the major defects of AM parts. Entrapment of gas during the building of the sample and incomplete fusion of particles due to insufficient supply of energy are the primary reasons for the formation of pores in parts prepared by SLM. The overall porosity was measured using the Archimedes principle and found to be 0.7 ± 0.5% for these plates, and the location specific porosity was examined using X-ray microcomputed tomography. Figure 3a

shows the projection of the 3D reconstructed view of the pores (in red color) in sub-volume of dimensions 747 × 746 × 1066 μm^3 for the plate, as revealed by X-ray microcomputed tomography. Distribution of frequency of equivalent diameter of pores is shown in Figure 3b. Most of pores have equivalent diameter less than 10 μm.

3.2. Structural and microstructural characterization

XRD patterns for AM, HT, and WR plates are compiled in Figure 4. Peaks observed in the XRD pattern of the XY and XZ surface of AM plate confirm the hexagonal close packed (HCP) structure of titanium without any match with those for the body centered cubic (BCC) structure (Liu et al., 2019b; Ni et al., 2020). HCP structure of titanium is found in both α and α′ phases with similar lattice parameters. The α′ martensite phase is a version of α phase supersaturated with β stabilizing vanadium. Either of these phases can be present in the AM material as the plates were subjected to stress relieving after fabrication by SLM. The absence of β peaks in the XRD pattern suggests that the AM microstructure comprises of the supersaturated α′ phase. After heat treatment, peaks of the β phase of titanium are seen along with those of α in the HT plate. The WR plate, also, exhibits the peaks of β phase along with those of α. FWHM values for AM, HT, and WR plate are calculated and compiled in Table S1. Higher values of FWHM in the AM plate suggest the possibility of strain in the plate, whereas FWHM for HT and WR plates are less than that of the AM plate.

The crystallographic texture in the AM, HT, and WR plates is shown using the BD-IPF plots in Figure 5. BD-IPF of AM shows weak texture with the build direction closely parallel to $[11\bar{2}0]$ direction. After heat treatment, $[11\bar{2}0]$ texture component is still visible, however weak. IPF of the WR plate shows that ND (normal direction) is parallel to [0002] direction. ND is the direction perpendicular to the rolling plane of the wrought plate.

The microstructure of AM material (Figure 6a) shows fine acicular laths all over the XY surface. Acicular morphology corroborates the XRD results that these are the α′ phase. On the

cross-sectional XZ surface (Figure 6b), large columnar grains are seen in which α′ laths have grown. These columnar grains grow in a direction nearly parallel to the build direction. The size of the prior β grains is 109 ± 19 μm, which is in good agreement with the results of other studies (Marco Simonelli et al., 2014). The HT plate exhibits bimodal microstructure, as shown in Figure 6c, with coarse and bigger plates of primary α (α_P), and alternate lamellae of the secondary α (α_S) and β phases. Quantification of HT microstructure yields 25% of the area as α_P and the rest consisting of α_S and β phase. WR also shows the bimodal microstructure, shown in Figure 6e, but contains 55% globular α_P. Signature of elongated but broken α_P are visible in the WR microstructure.

EBSD was done on the XY surface of the AM and HT plates, and the corresponding IPF maps are shown in Figure 7. The IPF map of AM confirms that α′ laths did not form as colonies. The IPF map of HT reveals that the lamellar α_S formed as colonies (clustering of α laths belonging to same crystallographic variants) after heat treatment. The orientations of the α lamellae are similar in a colony.

3.3. Mechanical Characterization

The surface hardness values of all three conditions are compiled in Table 2. On the AM plate, the hardness of the XY and YZ surfaces are similar and are reported for the XY surface only. After heat treatment, the hardness decreased from 430 ± 10 to 340 ± 15 HV. On the WR plate, hardness is 370 ± 30 HV.

Figure 8 plots the tensile behavior of the alloy from the plate in all three conditions. Values of ultimate tensile strength (UTS), 0.2% proof stress (taken as the yield strength, YS) and elongation to failure are compiled in Table 2. AM exhibits the highest UTS and YS but least elongation to failure. Tensile behavior of HT and WR are similar and exhibit large uniform plastic deformation prior to failure. Fractographs from the tensile specimens of AM, HT and

WR are presented in Figure 9. The fractographs clearly indicate features corresponding to brittle fracture as well as the features associated with plastic deformation for the AM plate that exhibited some amount of plastic deformation. Fractographs of the samples from the HT and WR plates show the features associated with quasi-ductile failure.

The maximum loading capacity and deflection values for all three conditions were determined from the 3-point bend tests. The results of the tests are summarized in Table 3. As seen from the plots in Figure 10, the AM bone plate exhibited some amount of plastic deformation in the 3-point bend test, corroborating the results of the tensile test. The maximum load carried by AM plate is 4.2 kN, whereas that of HT and WR is similar and equal to 3.2 and 3.4 kN, respectively. Central deflection of 11.4 and 14.0 mm prior to fracture was seen in the HT and WR bone plates, respectively. Figure S2 shows the plate after 3-point bend test and clearly indicate the achieved central deflection in HT plate as compared to AM and WR plates.

3.4. Electrochemical characterization

Potentiodynamic polarization curves are plotted for all three bone plates in Figure 11 and the critical parameters, calculated from polarization curve, are compiled in Table 4. E_{corr} of AM samples was comparable to HT and WR samples. I_{corr} values obtained from the polarization curve suggest that the corrosion rate of all plates is low and are all of the same order.

3.5. Biological characterization

The fluorescence values from the Alamar blue assay for cells on AM, HT and WR are plotted in Figure 12. The fluorescence values were increased steadily from day 1 to 4, and further by day 7 for the cells cultured on AM, HT, and WR. The constantly increasing cells numbers, conferring that the cell cultures were vital and proliferate on each sample. The large, steady increase in the cell numbers on AM, HT, and WR surfaces suggest that the cells are

metabolically healthy and highly proliferative, Thus, AM and HT bone plates are as cytocompatible as the WR plate surface.

The cytocompatibility was assessed using cytoskeletal staining. The cells were well adhered with spindle-like spreading on all three surfaces (Figure 13). The highly spread morphology of cells and well-developed cytoskeleton confirms healthy phenotype of the osteoblasts on all surfaces (Rabel et al., 2020). The increased presence of cells by day 7 corroborates results presented above and confirms the favorable cell-material interactions.

4. Discussion

Additive manufacturing of metallic implants offers several opportunities over conventional manufacturing, including the ability to prepare implants with complex geometries and architecture and the opportunity to tailor implants for patient-specific needs. Despite the advantage of near-net-shape manufacturing achieved by SLM, the non-equilibrium microstructures of the printed parts impart poor ductility and toughness thereby, compromising the biomechanical safety of the implanted device. Thus, post-printing processing such as heat treatment of the parts prepared by SLM could be used to transform the microstructure for enhancing their biomechanical performance.

Herein, model bone plates were designed and prepared by SLM. Additively manufactured bone plates can better conform to the curvature of bones and aid in the reconstruction of complex fractures that can vary significantly between patients. The porosity of the as-printed plates was calculated to be 0.7%. Some larges pores of ~ 71 μm were seen while the rest are much smaller. However, these are fewer and smaller as compared to those reported in many other studies (Carroll et al., 2015).

4.1 Phases and microstructure

XRD patterns and microstructural features confirmed the presence of fine laths of the α′ phase in AM plates. Long columnar grains of prior β are present on the YZ surface of the AM plate, which is characteristic of epitaxial growth in additive manufacturing. These columnar grains form due to successive layer deposition and grow opposite to the direction of maximum heat flow. The β phase forms first upon solidification of a melt pool, which is transformed to α′ phase due to the high cooling rate and follows the Burgers orientation relationships (BOR) (Wang et al., 2003). It is well known that 12 variants of α/α′ are possible from the β phase according to the Burgers relationships. As more variants of α′ are selected, the texture becomes weaker and vice versa. For the SLM process, it has been reported that all variants of α′ formed during β→ α′ phase transformation (Simonelli et al., 2014).

After heat treatment, the microstructure transformed into a bimodal microstructure consisting of a mixture of α_P, and lamellae of α_S and β phases. The mechanism underlying the formation of α_P has been described earlier by our group (Sabban et al., 2019). Briefly, α_P forms by thermal grooving and boundary splitting of α′ laths that is driven by the high density of dislocations intrinsically present in the laths of the AM material. The temperature range used for the repeated thermal cycling during the thermal treatment also affects the microstructure. The heating and cooling rates affect the volume fraction of α_P and α_S phases and thereby determine the bimodal microstructure. From DSC measurements, we determined the β-transus of the material to be 1017 °C (Figure S3). Based on our previous experience (Sabban et al., 2019), the cycling temperature range was set a little lower than this temperature to induce globularization.

IPF maps obtained from EBSD of AM and HT samples are shown in Figure 6. IPF map of AM (Figure 7 (a, b)) reveals that there is no colony formation as the laths have different orientations. IPF map of HT (Figure 7 (c, d)) on which IQ is imposed can help to distinguish

between α_P and α_S based on their morphology. α_S has lamellar morphology and alternate lamellae have the same orientation, which concludes the formation of colonies in the transformed β region in HT plate. Orientation of α_P and α_S are similar, as observed in the IPF map of HT (Figure 7d). This observation suggests that the α_S colony appears to have nucleated at the α_P/β interface and grew inside the high temperature β phase by following the Burgers orientation relationship (BOR). This behavior has been marked by arrows in Figure 7d. When heating to 975 °C, laths of random orientation retain their morphology and grow with cycling due to the elemental partitioning effect and will be termed as α_P. At 975 °C, the volume fraction of the β phase increases to 90% whereas the balance is the α phase (Katzarov et al., 2002). When cooled from this temperature, these α_P act as a nucleation site for α_S, which will have the same orientation as α_P and grows in the form of colonies. This is confirmed by the IPF map of the HT plate.

As stated earlier total 12 variants of α/α′ can form during β→α phase transformation. Any combination of two α variants will generate 144 possible combinations of α/α intervariant misorientation, out of which 12 are low angle grain boundaries (LAGB), and 132 are high angle grain boundaries (HAGB) (Wang et al., 2003). Due to crystallographic equivalence, these 132 combinations of HAGBs reduce to only 5 distinct HAGBs and are listed in Table 5. If all variants have same number of occurrences, then the ratio between these HAGBs is 2:3:2:2:1, and a divergence from this ratio will indicate variant selection (Obasi et al., 2012). Based on this ratio, the fraction of Type 2, 3, 4, 5, and 6 HAGBs are 18.2%, 36.4%, 18.2%, 18.2% and 9.1%, respectively, for ideal condition. To calculate percentage of these HAGBs, the length of axis/angle pairs are calculated, and then the percentage appearance is calculated for AM and HT samples. This percentage of these axis/angle pairs is plotted in Figure 14 and compared with that of the ideal percentage. We assumed that total length of given HAGBs is indicative of its number of occurrences. Type 4 and Type 2 HAGBs were more prominent (~ 47% and

25%, respectively) in AM as compared to other HAGBs. This trend of high fraction of Type 4 and Type 2 intervariant boundaries in fully martensitic microstructure of Ti64 has been observed in alloy produced by electron beam powder bed fusion (Haghdadi et al., 2020) and water quenched from above β transus temperature (Beladi et al., 2014). Percentage of Type 3, 5, and 6 is lower as compared to their ideal percentage. After heat treatment, percentage of Types 4 and 2 HAGBs decreased and that of other HAGBs increased and these percentages were closer to the percentages of their ideal distribution. This observation suggests that tendency of variant selection is weakened after heat treatment, and this leads to a decrease in texture intensity after heat treatment.

4.2. Mechanical behavior of plates

The AM alloy showed the highest UTS that arises due to its non-equilibrium microstructure. The obtained values of tensile strength and elongation are in good agreement with the literature (Cao et al., 2018; Kumar et al., 2018; Qiu et al., 2013b; M. Simonelli et al., 2014; Tao et al., 2018). Here, we observed UTS of 1368 ± 16 MPa, which is higher than 1274 ± 26 MPa reported earlier by us (Sabban et al., 2019). This difference can arise due to differences in microstructural features such as the size of α′ laths and minor differences in the alloy composition. Finer α′ laths result in higher strength of the alloy according to the Hall-Petch equation (Galarraga et al., 2017). Ductility of the AM material is limited as α′ laths contain dense dislocations within, which suggests that the AM material is heavily strained (Wu et al., 2016). As the material is already strained, it cannot accommodate additional plastic deformation and thus, exhibits poor ductility. Other reasons contributing to the lower ductility is the limitation of slip within a lath as the α′ laths have a different orientation.

Martensitic decomposition of α′ has been reported to vary between 575 to 800 ºC. For SLM, it is reported that when heated above 800 ºC for 6 h, α′ decomposes into the equilibrium phases, α and β (Cao et al., 2018). During heat treatment, V diffuses out to the boundaries of

the α laths, and slow cooling results in coarsening of the α laths. Repeated thermal cycling yields a bimodal microstructure eventually. This phase transformation from $\alpha' \rightarrow \alpha + \beta$ results in decreased strain in the material. The decrease in strain is revealed by the reduction in FWHM of HT as compared to the AM samples as shown in Table S1. Material, which is not strained, can accommodate more plastic deformation as compared to a material that is already strained. Although Elongation to failure of HT and WR are 24.3 ± 0.7 and 22.4 ± 1.4 respectively but plastic deformation of both conditions is similar. The strain in the tensile tests was not measured with an extensometer. As a result, the slope of the elastic region can become sensitive to small changes in gauge section dimensions of the tensile specimens. This effect can lead to differences in the slopes of the tensile curves shown in Figure 8. UTS of both HT and WR is 964 ± 56 and 1000 ± 22 respectively and statistically similar. Tensile tests confirm the significant improvement in ductility in HT plates which is comparable to WR.

Tensile fractographs of the AM alloy (Figure 9a) revealed rough surface in the center and shear lips or flattened surfaces at the edges of the fractured surface. A sheet of shallow dimples is observed close to the edges of the fractured surface. Notably, the crack leading to failure seems to have propagated across different laths with dissimilar orientation, and so step-like features are observed on the fractured surface (Figure 9b). In the end, as a result of excessive loading, the crack passed from the surface directly, and the specimen broke into two parts. This sudden propagation resulted in a flat surface at the edges of the sample as revealed in Figure 9a. Some secondary cracks are visible on the surface, suggesting that small pores have coalesced and became bigger pores and ultimately formed the cracks as the stress value increased (Krakhmalev et al., 2016). These cracks arise due to the role played by normal stress in tensile deformation (Kuruvilla et al., 2008). The secondary cracks left their signature over the fractured surface. In contrast, HT exhibit characteristic features of quasi-ductile failure. The complete fractured surface in HT (Figure 9(c, d)) is covered with dimple rupture in which few

large dimples (>20 μm) were seen, which possibly originated due to the presence of large pores in HT plate. A large Secondary crack is visible on WR fractured surface (Figure 9e) along with high rough surface (Figure 9f) in surrounding. Crack has grown initially and extended in direction perpendicular to loading direction along its width which has weaken the material in loading. As a result WR sample failed into two parts leaving the signature of secondary crack and rough region.

During orthopedic surgery, the surgeon often deforms the bone plates to match the contour of the bones. Whereas additively manufactured plates will have a better match with the curvature, some minor adjustments may be required during surgery. Moreover, once implanted, the plates can experience complex loading conditions involving a variety of tensile and compressive loads. Thus, the performance of the bone plates was assessed by means of the 3-point bend test. AM bone plates show poor bending capability and exhibit little plastic deformation behavior corroborating the results of the tensile test. On the other hand, WR plates were ductile with the maximum central deflection of more than 3 times compared to that of AM bone plates.

HT bone plates exhibited the same trend as the WR bone plates in the 3-point bend test. HT bone plates showed excellent bending capability with high central deflection prior to fracture and the similar maximum load bearing capacity as that of those of the WR plates. This test confirms the similar bending behavior of HT and WR plates under bending loads. The unique cyclic heat treatment applied here successfully yielded the bimodal microstructure, which is known to result in good tensile ductility, and herein, resulted in high deflection in the 3-point bend test (Sabban et al., 2019). These results concludes that additively manufactured plate's mechanical performance has significantly improved after subjecting it to heat treatment. Patient specific plates will experience minimum von misses stress field as compared to standard bone plates and will preserve the bone on loading (Didier et al., 2017). Such ductility is critical

for using the bone plates for contouring to large curvature bones such as the skull, pelvic, and spinal cord, etc. These deflection values scale with the observed tensile ductility, which indicates that increase in the ductility results in increase in deflection.

4.3. Electrochemical and biological behavior of plates

In addition to good mechanical properties, Ti-6Al-4V is a popular choice for biomedical implants due to its excellent corrosion resistance. We, thus, assessed the electrochemical properties of the additively manufactured plates and compared with the WR plate. Potentiodynamic curve can help in extracting useful parameters revealing the kinetics of corrosion. I_{corr} values of all three conditions are similar in this investigation. Contrary to our study, it has been reported in literature that the additively manufactured material shows poor corrosion resistance as compared to the wrought alloy in 3.5 wt.% NaCl solution (Dai et al., 2016; Hemmasian Ettefagh et al., 2019). According to these studies, α′ is a non-equilibrium phase of Ti, and has higher energy state as compared to the equilibrium phases (α and β) that results in low resistance to dissolution (Hemmasian Ettefagh et al., 2019). The single phase microstructure and stress relieving might have played a role in better corrosion resistance of the AM samples in our study, as has been proposed in some studies (Hemmasian Ettefagh et al., 2019). Magnitude of I_{corr} value of HT samples is marginally higher than the WR samples, which could be due to the variation of the fraction of the transformed β. The fraction of the transformed β is higher in HT as compared to the WR plate. This dual phase microstructure facilitates galvanic corrosion and increases the corrosion rate due to more α_S/β interfaces. In Ti alloys, it has been reported that higher fraction of the β phase imparts better corrosion resistance due to the more stable oxide film that is formed in comparison to the oxide on the α phase (Bai et al., 2017; Hemmasian Ettefagh et al., 2019; Toptan et al., 2019). Increase in the transformed β area fraction also increases the chances of galvanic corrosion between two

phases present in the microstructure, which could be responsible for the marginally higher magnitude of I_{corr} value of the HT samples.

The cytocompatibility was assessed *in vitro* using MC3T3-E1 mouse calvarial pre-osteoblasts, which is a well-established osteoblast model (Czekanska et al., 2012). The steady cell growth (Figure 12) confirmed that there is no cytotoxicity associated with all the three types of plates. Good biocompatibility of additively manufactured Ti64, as accessed through i*n-vitro* in current work, is consistent with other reported work on additive manufacturing of this alloy (Lin et al., 2018; Shah et al., 2016). Fluorescence intensity of AM is marginally higher at day 1 as compared to HT and WR plates which suggest that cells are attaching to AM samples easily. While at day 4 Fluorescence intensity of HT and WR is marginally higher as compared to AM samples which suggest that cell proliferation is faster on these samples. This different cell response of AM as compared to HT and WR could be due to changes in oxide composition and properties on HT and WR samples as they have both β and α phases while AM has only α′ phase. It is reported in literature that surface roughness and oxide film layer properties could affect the cell response. All the samples used in biological study are electropolished and have same roughness values therefore eliminates any possible role played by roughness on different cell response. The formation of dual phase microstructure in WR and HT, results into existence of both the α and β phases with significant different compositions, could change the composition and properties of the oxide layer (Bahl et al., 2017, 2015). This changes in oxide layer could have played a role in different cell response of AM samples in this study (Bahl et al., 2018). At Day 7, cells achieved confluency on the surfaces of AM, HT and WR plates.

The morphological analysis revealed characteristic cell spreading of the osteoblasts on AM, HT and WR samples. WR plates of Ti-6Al-4V were expected to be cytocompatible given their widespread clinical use. Although biocompatibility of AM Ti64 is reported in few studies

but reports on heat treated AM Ti64 parts is not available (Thomsen et al., 2009; Wang et al., 2016). Our work on heat treatment of additively manufactured plates concludes that there is no cytotoxicity associated with these plates after subjecting them to heat treatment as compared to WR. The HT plates are equally cytocompatible as WR plates as all are showing that cells are proliferating on them as shown in Figure 12. Thus, heat treatment of these bone plates could not only improve its mechanical properties but also increases its cytocompatibility.

Taken together the results of this study suggest that near-net-shape manufacturing by SLM offers a feasible route to prepare patient-specific bone plates. The cyclic heat treatment schedule yields a bimodal microstructure and improves the ductility of the bone plate that is similar to bone plates prepared by machining of wrought material without compromising the corrosion resistance and cytocompatibility. Thus, the HT bone plates combine the advantage of personalized medical devices with excellent biomechanical performance. Although we have prepared bone plates of a simple design in this work as proof of concept, it is envisaged that this strategy can be applied for other additively manufactured Ti-6Al-4V implants of complex geometry.

5. Conclusion

Bone plates were prepared by SLM of Ti-6Al-4V and subjected to a cyclic heat treatment to achieve good biomechanical performance comparable to that of WR bone plates. The microstructure of the AM bone plates consists of martensitic laths imparting high strength, but poor ductility. HT plates exhibit bimodal microstructure with good ductility similar to those of WR plates. HT did not markedly alter the texture of the AM plate and the major orientations in build directions continued to be parallel to $<11\bar{2}0>$. Unlike the brittle AM plate, both HT and WR plates exhibit high deflection and same maximum load in the 3-point bend test. The corrosion resistance of the material is similar before and after heat treatment, and comparable to the wrought plate. *In vitro* cytocompatibility was similar for AM, HT, and WR plates. These

results suggest that patient-specific implants can be prepared by SLM of Ti-6Al-4V without compromising their biomechanical performance by subjecting them to this cyclic heat treatment.

Acknowledgements

The authors gratefully acknowledge funding from Uchchatar Avishkar Yojana Program (IISc_004) and the Bioengineering and Biodesign Initiative Phase 2 supported by the Department of Biotechnology (DBT), India. PKDVY acknowledges funding from the VAJRA program of the Science and Engineering Research Board (SERB), India. DK acknowledges D.S. Kothari Fellowship from the University Grants Commission of India. Help from Dr. Santanu Ghosh with cell studies is gratefully acknowledged.

References

Ali, H., Ghadbeigi, H., Mumtaz, K., 2018. Processing Parameter Effects on Residual Stress and Mechanical Properties of Selective Laser Melted Ti6Al4V. J. Mater. Eng. Perform. 27, 4059–4068. https://doi.org/10.1007/s11665-018-3477-5

Bahl, S., Aleti, B.T., Suwas, S., Chatterjee, K., 2018. Surface nanostructuring of titanium imparts multifunctional properties for orthopedic and cardiovascular applications. Mater. Des. 144, 169–181. https://doi.org/10.1016/j.matdes.2018.02.022

Bahl, S., Krishnamurthy, A.S., Suwas, S., Chatterjee, K., 2017. Controlled nanoscale precipitation to enhance the mechanical and biological performances of a metastable β Ti-Nb-Sn alloy for orthopedic applications. Mater. Des. 126, 226–237. https://doi.org/10.1016/j.matdes.2017.04.014

Bahl, S., Shreyas, P., Trishul, M.A., Suwas, S., Chatterjee, K., 2015. Enhancing the mechanical and biological performance of a metallic biomaterial for orthopedic applications through changes in the surface oxide layer by nanocrystalline surface modification. Nanoscale 7, 7704–7716. https://doi.org/10.1039/c5nr00574d

Bahl, S., Suwas, S., Chatterjee, K., 2014. The importance of crystallographic texture in the use of titanium as an orthopedic biomaterial 38078–38087. https://doi.org/10.1039/c4ra05440g

Bai, Y., Gai, X., Li, S., Zhang, L.C., Liu, Y., Hao, Y., Zhang, X., Yang, R., Gao, Y., 2017. Improved corrosion behaviour of electron beam melted Ti-6Al–4V alloy in phosphate buffered saline. Corros. Sci. 123, 289–296. https://doi.org/10.1016/j.corsci.2017.05.003

Beladi, H., Chao, Q., Rohrer, G.S., 2014. Variant selection and intervariant crystallographic planes distribution in martensite in a Ti-6Al-4V alloy. Acta Mater. 80, 478–489. https://doi.org/10.1016/j.actamat.2014.06.064

Cao, S., Chu, R., Zhou, X., Yang, K., Jia, Q., Lim, C.V.S., Huang, A., Wu, X., 2018. Role of martensite decomposition in tensile properties of selective laser melted Ti-6Al-4V. J. Alloys Compd. 744, 357–363. https://doi.org/10.1016/j.jallcom.2018.02.111

Carroll, B.E., Palmer, T.A., Beese, A.M., 2015. Anisotropic tensile behavior of Ti-6Al-4V components fabricated with directed energy deposition additive manufacturing. Acta Mater. 87, 309–320. https://doi.org/10.1016/j.actamat.2014.12.054

Czekanska, E.M., Stoddart, M.J., Richards, R.G., Hayes, J.S., 2012. In search of an osteoblast cell model for in vitro research. Eur. Cells Mater. 24, 1–17. https://doi.org/10.22203/eCM.v024a01

Dai, N., Zhang, L.C., Zhang, J., Chen, Q., Wu, M., 2016. Corrosion behavior of selective laser

melted Ti-6Al-4V alloy in NaCl solution. Corros. Sci. 102, 484–489. https://doi.org/10.1016/j.corsci.2015.10.041

Didier, P., Piotrowski, B., Fischer, M., Laheurte, P., 2017. Mechanical stability of custom-made implants: Numerical study of anatomical device and low elastic Young's modulus alloy. Mater. Sci. Eng. C 74, 399–409. https://doi.org/10.1016/j.msec.2016.12.031

Fan, Z., Feng, H., 2018. Study on selective laser melting and heat treatment of Ti-6Al-4V alloy. Results Phys. 10, 660–664. https://doi.org/10.1016/j.rinp.2018.07.008

Fang, Z.Z., Paramore, J.D., Sun, P., Chandran, K.S.R., Zhang, Y., Xia, Y., Cao, F., Koopman, M., Free, M., 2018. Powder metallurgy of titanium–past, present, and future. Int. Mater. Rev. 63, 407–459. https://doi.org/10.1080/09506608.2017.1366003

Frazier, W.E., 2014. Metal additive manufacturing: A review. J. Mater. Eng. Perform. https://doi.org/10.1007/s11665-014-0958-z

Galarraga, H., Warren, R.J., Lados, D.A., Dehoff, R.R., Kirka, M.M., Nandwana, P., 2017. Effects of heat treatments on microstructure and properties of Ti-6Al-4V ELI alloy fabricated by electron beam melting (EBM). Mater. Sci. Eng. A 685, 417–428. https://doi.org/10.1016/j.msea.2017.01.019

Geetha, M., Singh, A.K., Asokamani, R., Gogia, A.K., 2009. Ti based biomaterials , the ultimate choice for orthopaedic implants – A review. Prog. Mater. Sci. 54, 397–425. https://doi.org/10.1016/j.pmatsci.2008.06.004

Global Trauma Fixation Devices Market 2017-2021, 2017.

Haghdadi, N., DeMott, R., Stephenson, P.L., Liao, X.Z., Ringer, S.P., Primig, S., 2020. Five-parameter characterization of intervariant boundaries in additively manufactured Ti-6Al-4V. Mater. Des. 196, 109177. https://doi.org/10.1016/j.matdes.2020.109177

Harith, H., Malekani, J., Schmutz, B., Schuetz, M., Yarlagadda, P.K.D.V., 2016. A method for optimal fit of patient-specific fracture fixation plates. Proc. Inst. Mech. Eng. Part L J. Mater. Des. Appl. 230, 282–290. https://doi.org/10.1177/1464420715569586

Harith, H.H., Malekani, J., Schmutz, B., Schuetz, M., 2014. A Novel Iterative Method for Simulating Patient-Specific Optimal Deformation and Fit of Fracture Fixation Plates 845, 382–386. https://doi.org/10.4028/www.scientific.net/AMR.845.382

Hemmasian Ettefagh, A., Zeng, C., Guo, S., Raush, J., 2019. Corrosion behavior of additively manufactured Ti-6Al-4V parts and the effect of post annealing. Addit. Manuf. 28, 252–258. https://doi.org/10.1016/j.addma.2019.05.011

Kasperovich, G., Haubrich, J., Gussone, J., Requena, G., 2016. Correlation between porosity and processing parameters in TiAl6V4 produced by selective laser melting. Mater. Des. 105, 160–170. https://doi.org/10.1016/j.matdes.2016.05.070

Katzarov, I., Malinov, S., Sha, W., 2002. Finite element modeling of the morphology of β to α phase transformation in Ti-6Al-4V alloy. Metall. Mater. Trans. A Phys. Metall. Mater. Sci. 33, 1027–1040. https://doi.org/10.1007/s11661-002-0204-4

Krakhmalev, P., Fredriksson, G., Yadroitsava, I., Kazantseva, N., Du Plessis, A., Yadroitsev, I., 2016. Deformation behavior and microstructure of Ti6Al4V manufactured by SLM. Phys. Procedia 83, 778–788. https://doi.org/10.1016/j.phpro.2016.08.080

Kumar, P., Prakash, O., Ramamurty, U., 2018. Micro-and meso-structures and their influence on mechanical properties of selectively laser melted Ti-6Al-4V. Acta Mater. 154, 246–260. https://doi.org/10.1016/j.actamat.2018.05.044

Kurtz, S., Ong, K., Lau, E., Mowat, F., Halpern, M., 2007. Projections of primary and revision hip and knee arthroplasty in the United States from 2005 to 2030. J. Bone Jt. Surg. - Ser.

A 89, 780–785. https://doi.org/10.2106/JBJS.F.00222

Kuruvilla, M., Srivatsan, T.S., Petraroli, M., Park, L., 2008. An investigation of microstructure, hardness, tensile behaviour of a titanium alloy: Role of orientation. Sadhana - Acad. Proc. Eng. Sci. 33, 235–250. https://doi.org/10.1007/s12046-008-0017-2

Lin, X., Xiao, X., Wang, Y., Gu, C., Wang, C., Chen, J., Liu, H., Luo, J., Li, T., Wang, D., Fan, S., 2018. Biocompatibility of Bespoke 3D-Printed Titanium Alloy Plates for Treating Acetabular Fractures. Biomed Res. Int. 2018. https://doi.org/10.1155/2018/2053486

Liu, J., Sun, Q., Zhou, C., Wang, X., Li, H., Guo, K., Sun, J., 2019a. Achieving Ti6Al4V alloys with both high strength and ductility via selective laser melting. Mater. Sci. Eng. A 766. https://doi.org/10.1016/j.msea.2019.138319

Liu, J., Sun, Q., Zhou, C., Wang, X., Li, H., Guo, K., Sun, J., 2019b. Achieving Ti6Al4V alloys with both high strength and ductility via selective laser melting. Mater. Sci. Eng. A. https://doi.org/10.1016/j.msea.2019.138319

Liu, S., Shin, Y.C., 2019. Additive manufacturing of Ti6Al4V alloy: A review. Mater. Des. 164, 107552. https://doi.org/10.1016/j.matdes.2018.107552

Ngo, T.D., Kashani, A., Imbalzano, G., Nguyen, K.T.Q., Hui, D., 2018. Additive manufacturing (3D printing): A review of materials , methods , applications and challenges. Compos. Part B 143, 172–196. https://doi.org/10.1016/j.compositesb.2018.02.012

Ni, C., Zhu, L., Zheng, Z., Zhang, J., Yang, Y., Yang, J., Bai, Y., Weng, C., Lu, W.F., Wang, H., 2020. Effect of material anisotropy on ultra-precision machining of Ti-6Al-4V alloy fabricated by selective laser melting. J. Alloys Compd. 848, 156457. https://doi.org/10.1016/j.jallcom.2020.156457

Obasi, G.C., Birosca, S., Quinta Da Fonseca, J., Preuss, M., 2012. Effect of β grain growth on variant selection and texture memory effect during α → β → α phase transformation in Ti-6 Al-4 v. Acta Mater. 60, 1048–1058. https://doi.org/10.1016/j.actamat.2011.10.038

Qiu, C., Adkins, N.J.E., Attallah, M.M., 2013a. Microstructure and tensile properties of selectively laser-melted and of HIPed laser-melted Ti-6Al-4V. Mater. Sci. Eng. A 578, 230–239. https://doi.org/10.1016/j.msea.2013.04.099

Qiu, C., Adkins, N.J.E., Attallah, M.M., 2013b. Microstructure and tensile properties of selectively laser-melted and of HIPed laser-melted Ti-6Al-4V. Mater. Sci. Eng. A 578, 230–239. https://doi.org/10.1016/j.msea.2013.04.099

Rabel, K., Kohal, R.J., Steinberg, T., Tomakidi, P., Rolauffs, B., Adolfsson, E., Palmero, P., Fürderer, T., Altmann, B., 2020. Controlling osteoblast morphology and proliferation via surface micro-topographies of implant biomaterials. Sci. Rep. 10, 1–14. https://doi.org/10.1038/s41598-020-69685-6

Sabban, R., Bahl, S., Chatterjee, K., Suwas, S., 2019. Globularization using heat treatment in additively manufactured Ti-6Al-4V for high strength and toughness. Acta Mater. 162, 239–254. https://doi.org/10.1016/j.actamat.2018.09.064

Shah, F.A., Snis, A., Matic, A., Thomsen, P., Palmquist, A., 2016. 3D printed Ti6Al4V implant surface promotes bone maturation and retains a higher density of less aged osteocytes at the bone-implant interface. Acta Biomater. 30, 357–367. https://doi.org/10.1016/j.actbio.2015.11.013

Simonelli, Marco, Tse, Y.Y., Tuck, C., 2014. On the texture formation of selective laser melted Ti-6Al-4V. Metall. Mater. Trans. A Phys. Metall. Mater. Sci. 45, 2863–2872. https://doi.org/10.1007/s11661-014-2218-0

Simonelli, M., Tse, Y.Y., Tuck, C., 2014. Effect of the build orientation on the mechanical properties and fracture modes of SLM Ti-6Al-4V. Mater. Sci. Eng. A 616, 1–11. https://doi.org/10.1016/j.msea.2014.07.086

Tao, P., Li, H. xue, Huang, B. ying, Hu, Q. dong, Gong, S. li, Xu, Q. yan, 2018. Tensile behavior of Ti-6Al-4V alloy fabricated by selective laser melting: effects of microstructures and as-built surface quality. China Foundry 15, 243–252. https://doi.org/10.1007/s41230-018-8064-8

Ter Haar, G.M., Becker, T.H., 2018. Selective laser melting produced Ti-6Al-4V: Post-process heat treatments to achieve superior tensile properties. Materials (Basel). 11. https://doi.org/10.3390/ma11010146

Thomsen, P., Malmström, J., Emanuelsson, L., René, M., Snis, A., 2009. Electron beam-melted, free-form-fabricated titanium alloy implants: Material surface characterization and early bone response in rabbits. J. Biomed. Mater. Res. - Part B Appl. Biomater. 90 B, 35–44. https://doi.org/10.1002/jbm.b.31250

Toptan, F., Alves, A.C., Carvalho, Ó., Bartolomeu, F., Pinto, A.M.P., Silva, F., Miranda, G., 2019. Corrosion and tribocorrosion behaviour of Ti6Al4V produced by selective laser melting and hot pressing in comparison with the commercial alloy. J. Mater. Process. Technol. 266, 239–245. https://doi.org/10.1016/j.jmatprotec.2018.11.008

Vrancken, B., Thijs, L., Kruth, J., Humbeeck, J. Van, 2012. Heat treatment of Ti6Al4V produced by Selective Laser Melting : Microstructure and mechanical properties. J. Alloys Compd. 541, 177–185. https://doi.org/10.1016/j.jallcom.2012.07.022

Wang, H., Zhao, B., Liu, C., Wang, C., Tan, X., Hu, M., 2016. A comparison of biocompatibility of a titanium alloy fabricated by electron beam melting and selective laser melting. PLoS One 11, 1–19. https://doi.org/10.1371/journal.pone.0158513

Wang, S.C., Aindow, M., Starink, M.J., 2003. Effect of self-accommodation on α/α boundary populations in pure titanium. Acta Mater. 51, 2485–2503. https://doi.org/10.1016/S1359-6454(03)00035-1

Wu, S.Q., Lu, Y.J., Gan, Y.L., Huang, T.T., Zhao, C.Q., Lin, J.J., Guo, S., Lin, J.X., 2016. Microstructural evolution and microhardness of a selective-laser-melted Ti-6Al-4V alloy after post heat treatments. J. Alloys Compd. 672, 643–652. https://doi.org/10.1016/j.jallcom.2016.02.183

Yang, J., Yu, H., Yin, J., Gao, M., Wang, Z., Zeng, X., 2016. Formation and control of martensite in Ti-6Al-4V alloy produced by selective laser melting. Mater. Des. 108, 308–318. https://doi.org/10.1016/j.matdes.2016.06.117

Table 1 *Processing parameters for SLM*

Equipment and Laser type	Renishaw AM400 and 400 W Ytterbium fiber laser
Exact laser beam/ spot size	70 µm
Building chamber volume	250 X 250 X 300 mm^3
Laser power	200 W
Laser scan speed	800 mm/s
Laser exposure time	70 µs
Powder layer thickness	40 µm
Feed powder size distribution	20 to 60 µm
Build density	Established based on the samples
Hatch size	70 µm
Scanning strategy	Meander

Table 2 *Mechanical properties in tensile loading*

Specimen	**Yield Strength (MPa)**	**Tensile Strength (MPa)**	**Elongation to failure (%)**	**Hardness (HV)**
AM	1287 ± 10	1367 ± 14	11.5 ± 1.5	430 ± 10
HT	743 ± 19	964 ± 56	24.3 ± 0.7	330 ± 20
WR	859 ± 7	1000 ± 22	22.4 ± 1.4	370 ± 30

All data are mean ± S.D. for $n \geq 3$

Table 3 *Fracture properties in 3-point bend test*

Specimen	Fracture load (kN)	Maximum deflection (mm)
AM	4.2 ± 0.5	5.7 ± 1.4
HT	3.2 ± 0	11.4 ± 0.3
WR	3.4 ± 0.1	14.0 ± 1.7

All data are mean ± S.D. for $n \geq 3$

Table 4 *Electrochemical properties*

Specimen	**E_{corr} (V vs. SCE)**	**I_{corr} (10^{-9}A.cm^{-2})**
AM	-0.3 ± 0.1	4.2 ± 2.3
HT	-0.4 ± 0.1	6.1 ± 1.1
WR	-0.4 ± 0.1	4.4 ± 0.1

All data are mean ± S.D. for n ≥ 3

Table 5 *Axis angle pairs between α/α variants*

Type of HAGBs	Axis angle pair
1	I
2	$[11\bar{2}0]/60°$
3	$[\overline{1.377}\ \ \bar{1}\ \ 2.377\ \ 0.359]/60.83°$
4	$[\overline{10}\ 5\ 5\ \bar{3}]/63.26°$
5	$[1\ \overline{2.38}\ \ 1.38\ 0/90°$
6	[0 0 0 1]/ 10.53°

Figure 1

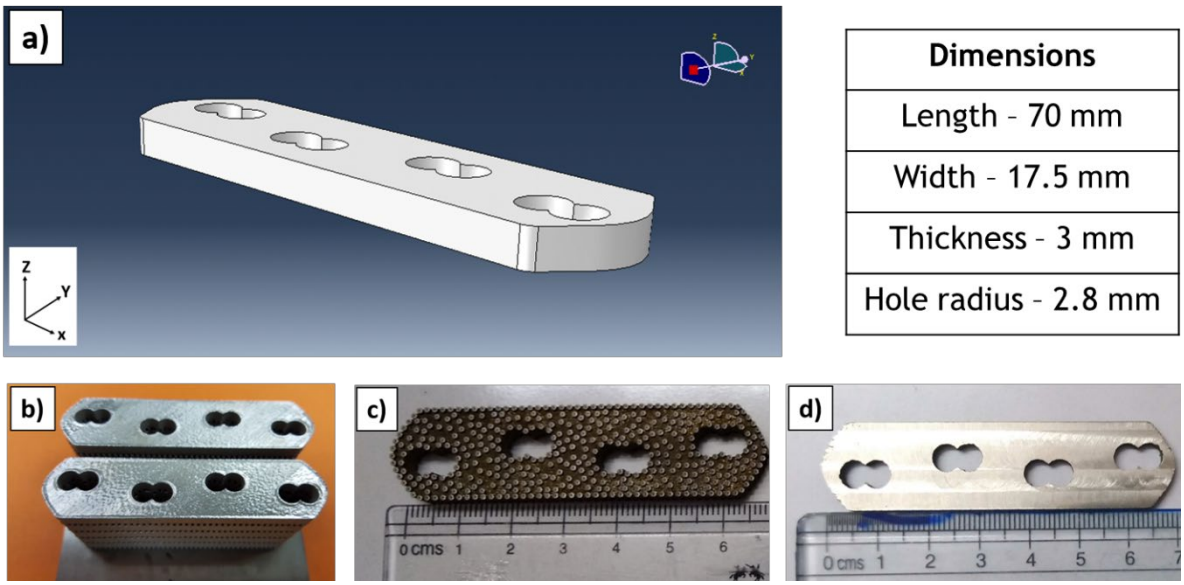

Dimensions
Length - 70 mm
Width - 17.5 mm
Thickness - 3 mm
Hole radius - 2.8 mm

Figure 1 *Additively manufactured bone plate: (a) CAD model (b) assembly of as-prepared plates (c) after stress relieving (d) after milling*

Figure 2

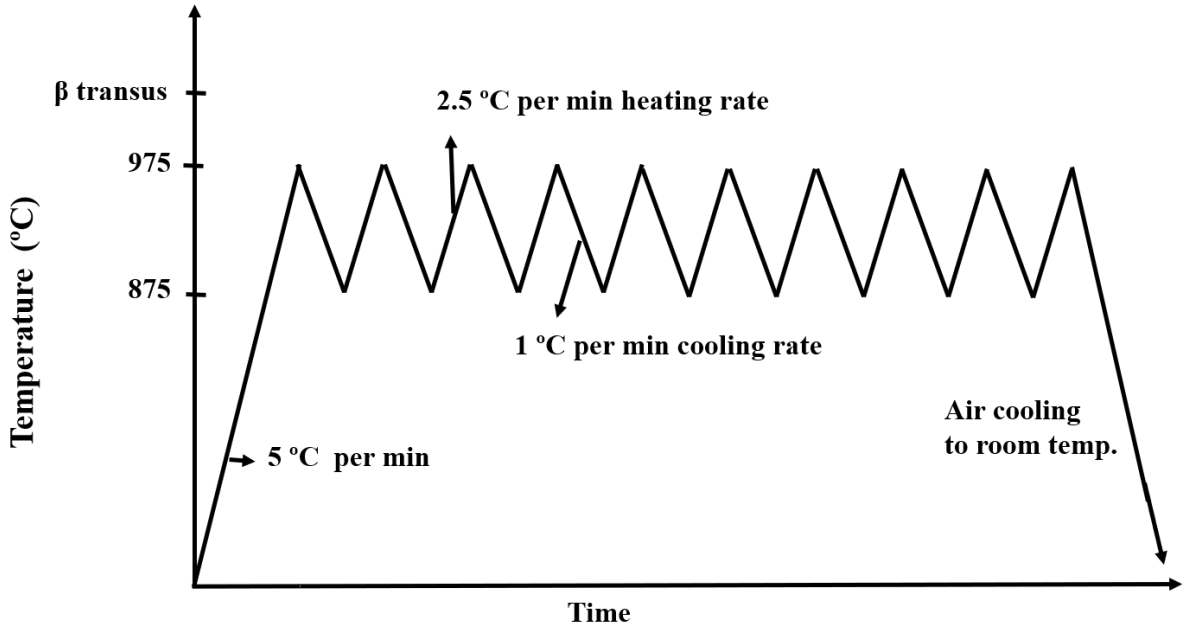

Figure 2 *Cyclic heat treatment schedule applied to the AM bone plates.*

Figure 3

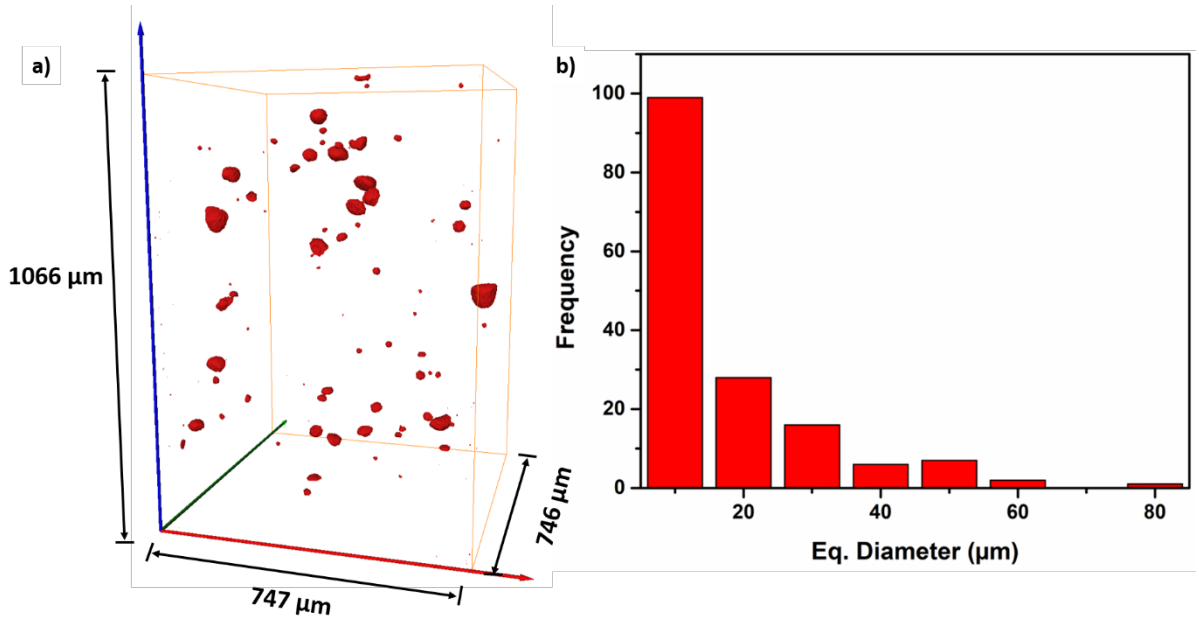

Figure 3 *(a) X-ray tomogram of the AM plate shows the presence of voids, (b) frequency distribution of equivalent pore diameter*

Figure 4

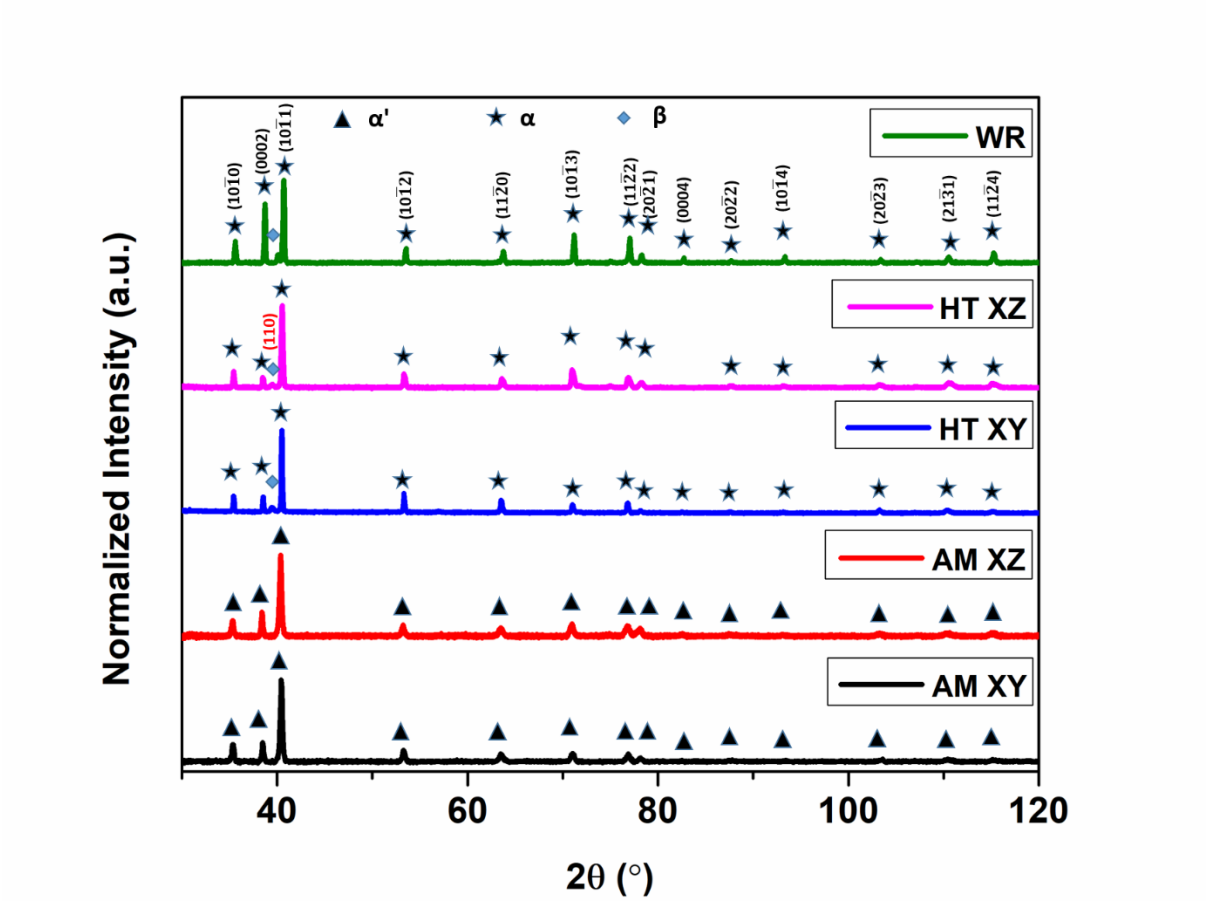

Figure 4 *Indexed XRD pattern of AM showing peaks of α' phase alone and that of HT and WR showing peaks of both α and β phases*

Figure 5

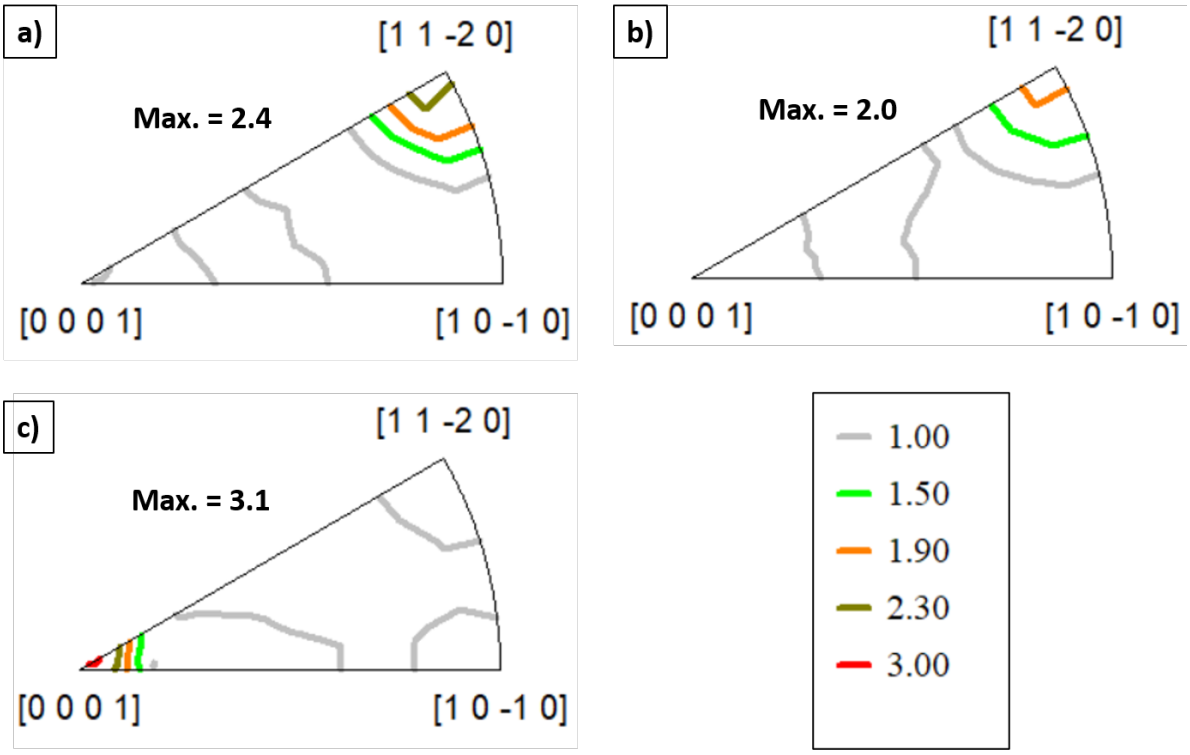

Figure 5 *BD - Inverse pole figures (IPFs) of (a) AM, (b) HT, and c) WR plate*

Figure 6

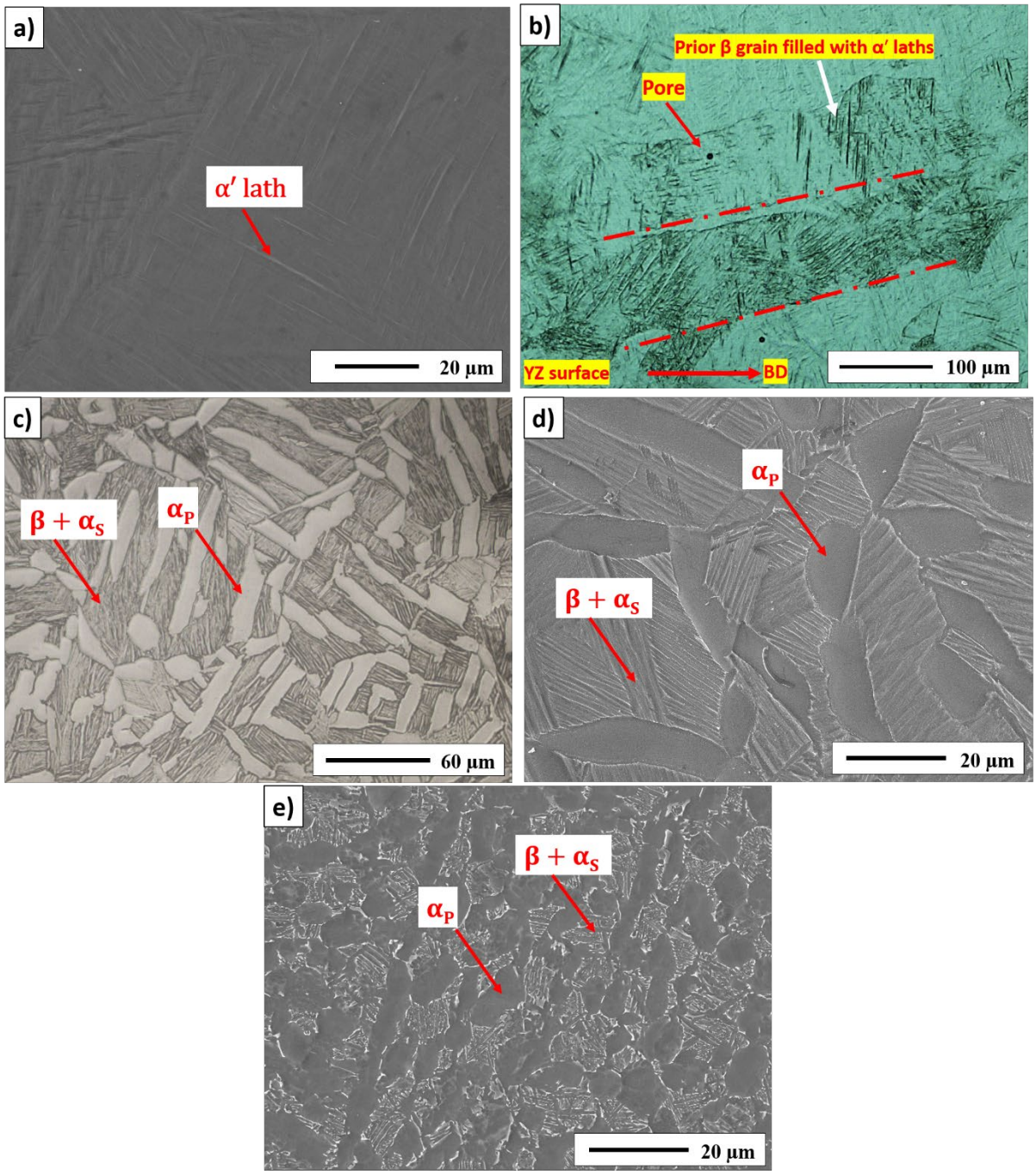

Figure 6 *(a) SEM micrographs of XY plane of AM plate showing laths, (b) Optical micrograph of the YZ plane showing epitaxial growth and columnar grains, (c) optical micrograph of HT showing primary α and lamellae of β and secondary α, (d, e) SEM micrograph of (d) HT plate and (e) WR plate showing bimodal microstructure*

Figure 7

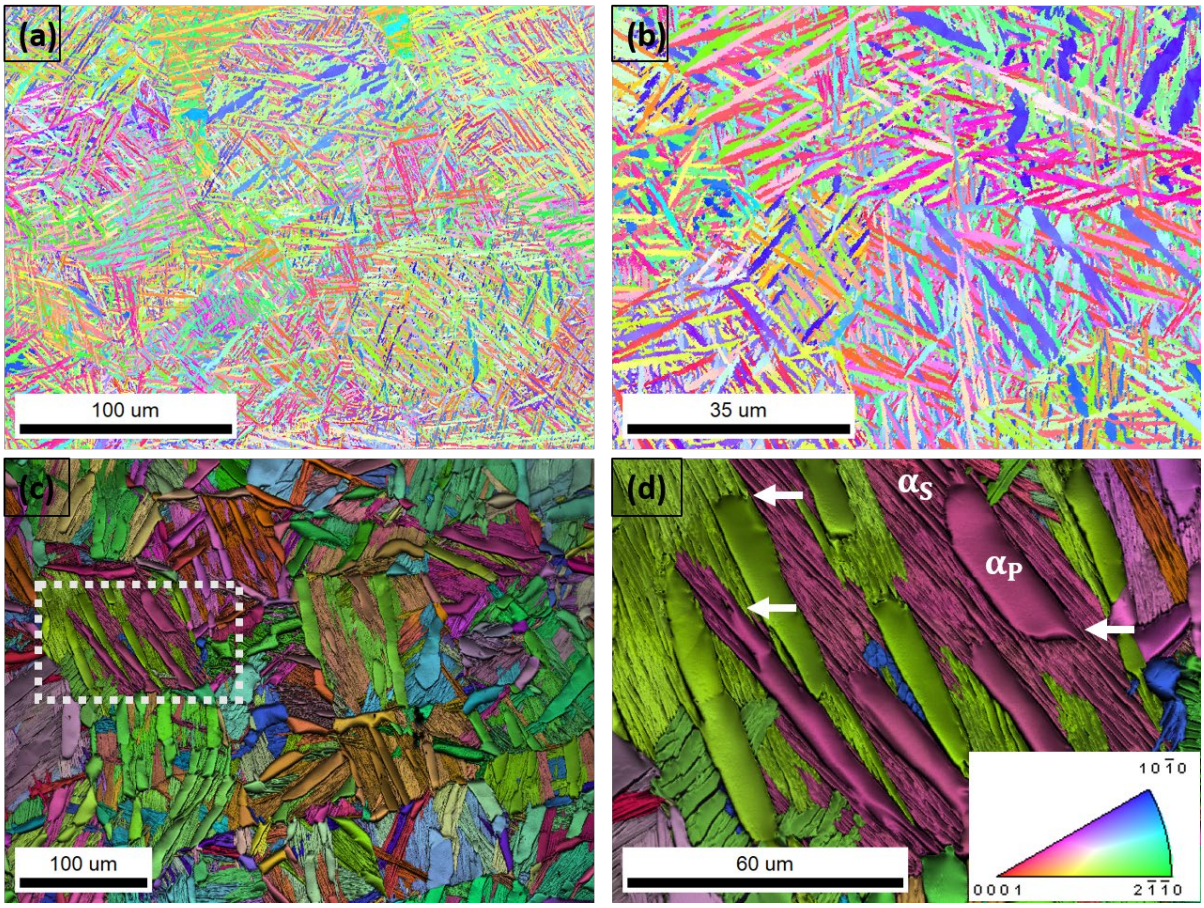

Figure 7 *(a, b) IPF map of AM sample and (c, d) IQ + IPF map of HT sample. Arrow indicates the nucleation of* $\boldsymbol{\alpha_S}$ *from* $\boldsymbol{\alpha_P}$

Figure 8

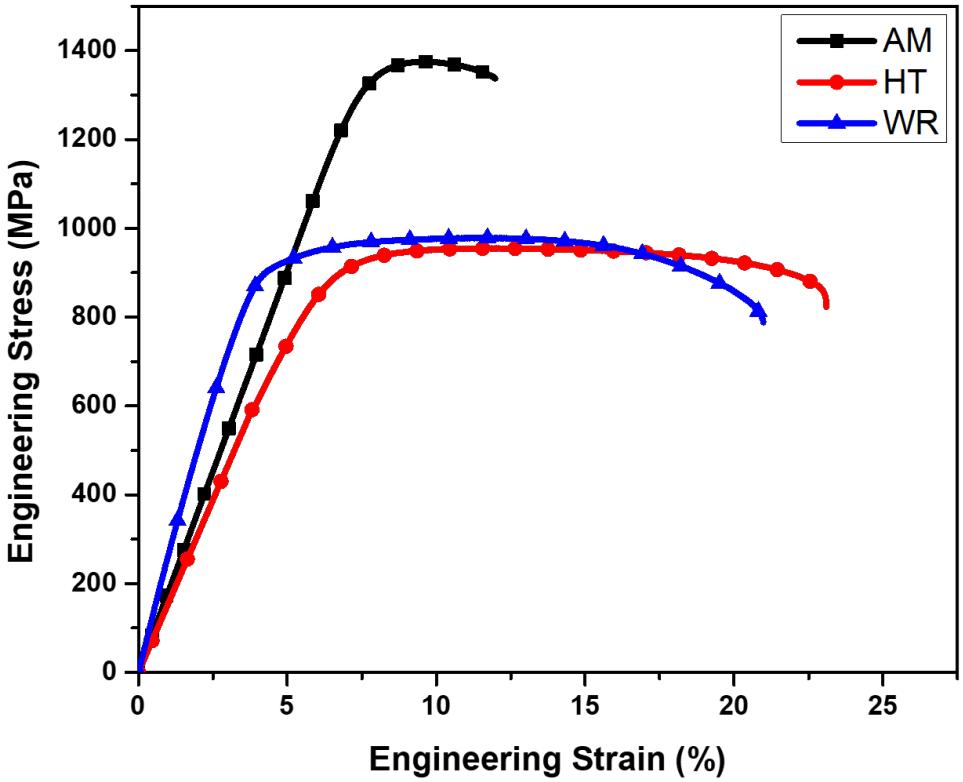

Figure 8 *Tensile plots for AM, HT, and WR bone plates*

Figure 9

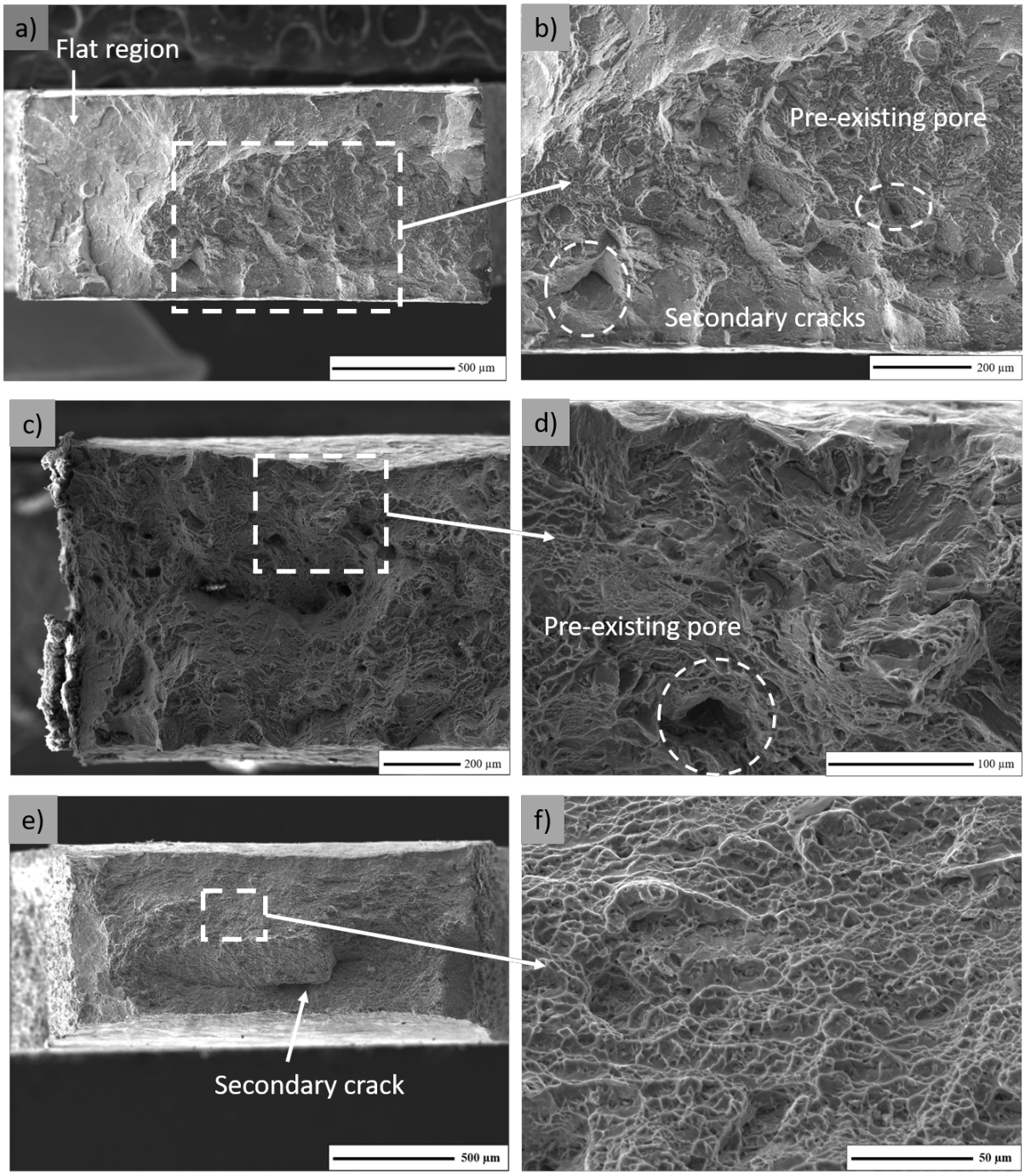

Figure 9 Secondary electron SEM images of fractured surfaces of (a and b) AM, (c and d) HT and (e and f) WR plates

Figure 10

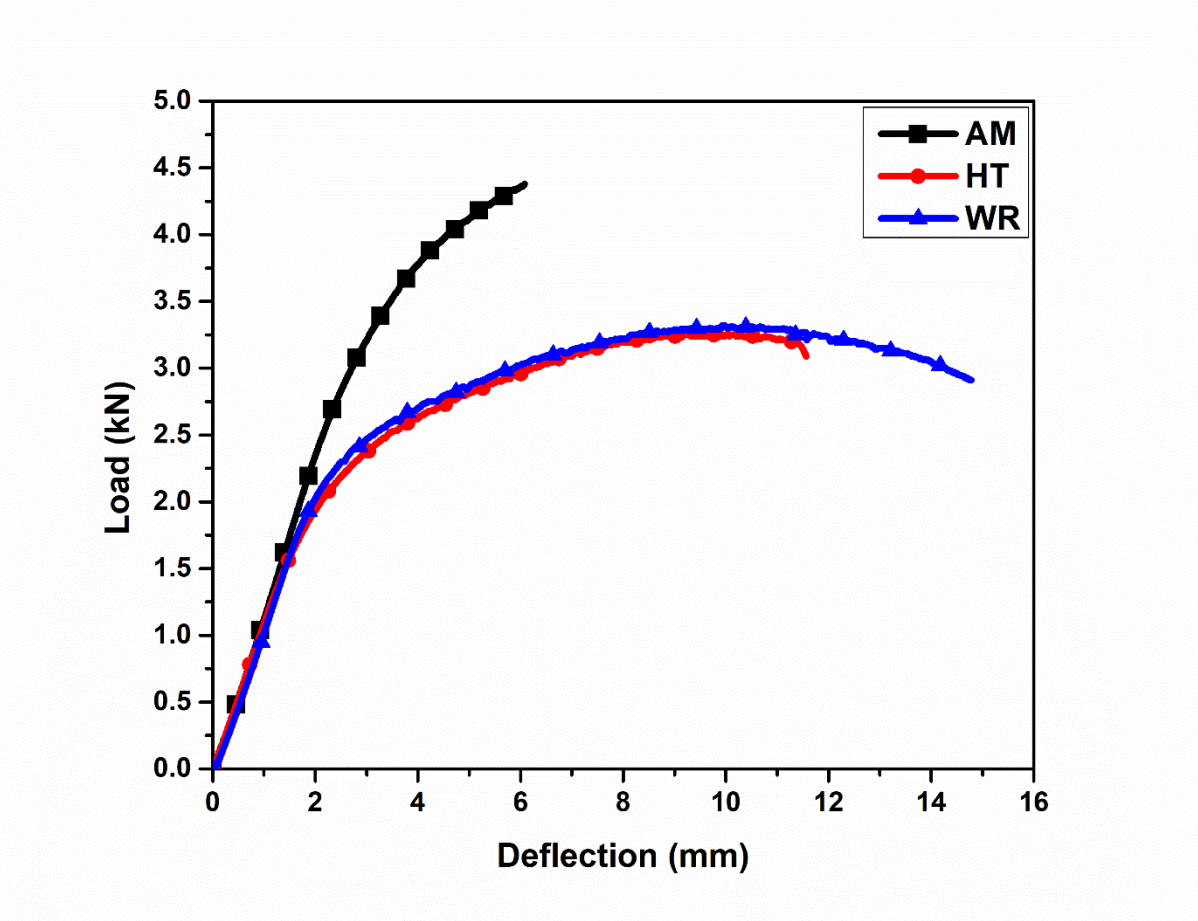

Figure 10 *Plots for 3-point bend test for AM, HT and WR bone plates*

Figure 11

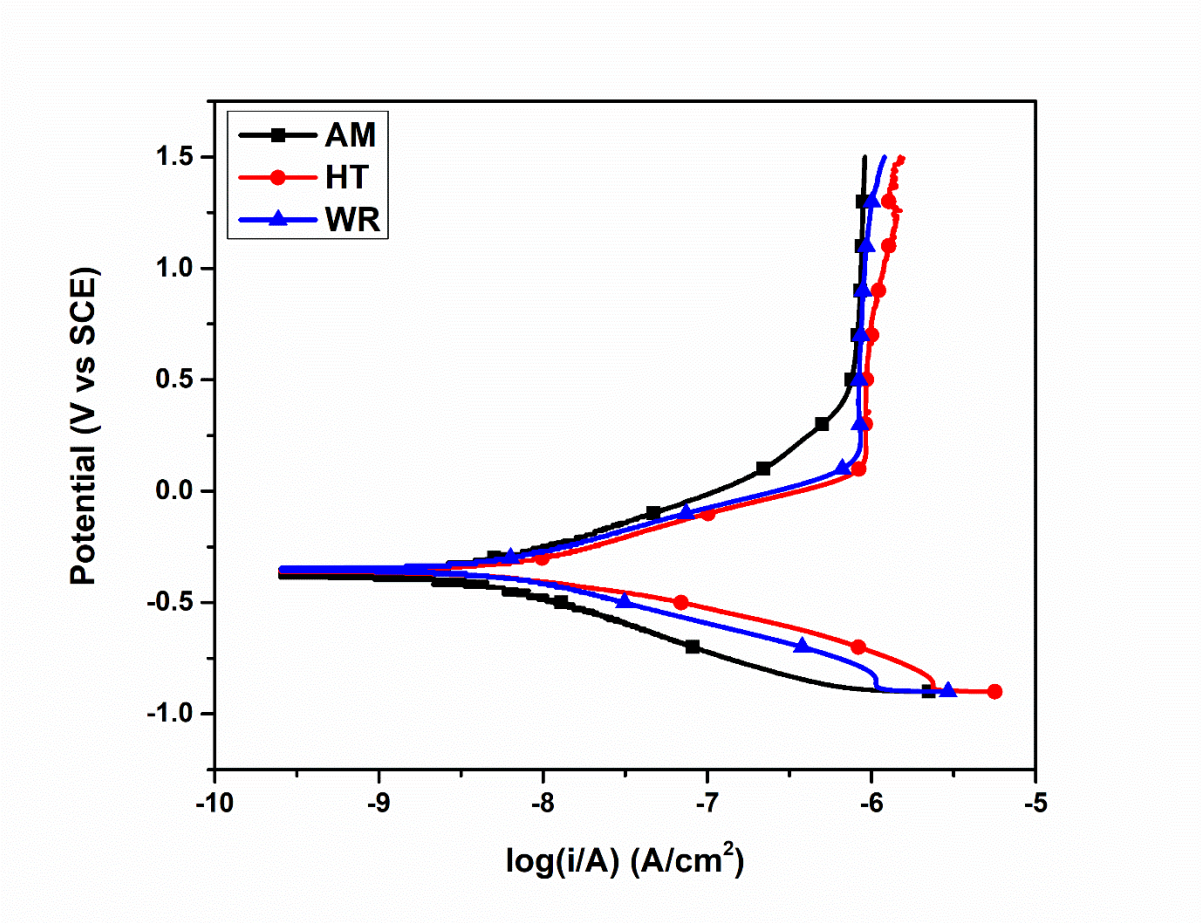

Figure 11 *Potentiodynamic curves for AM, HT and WR in SBF.*

Figure 12

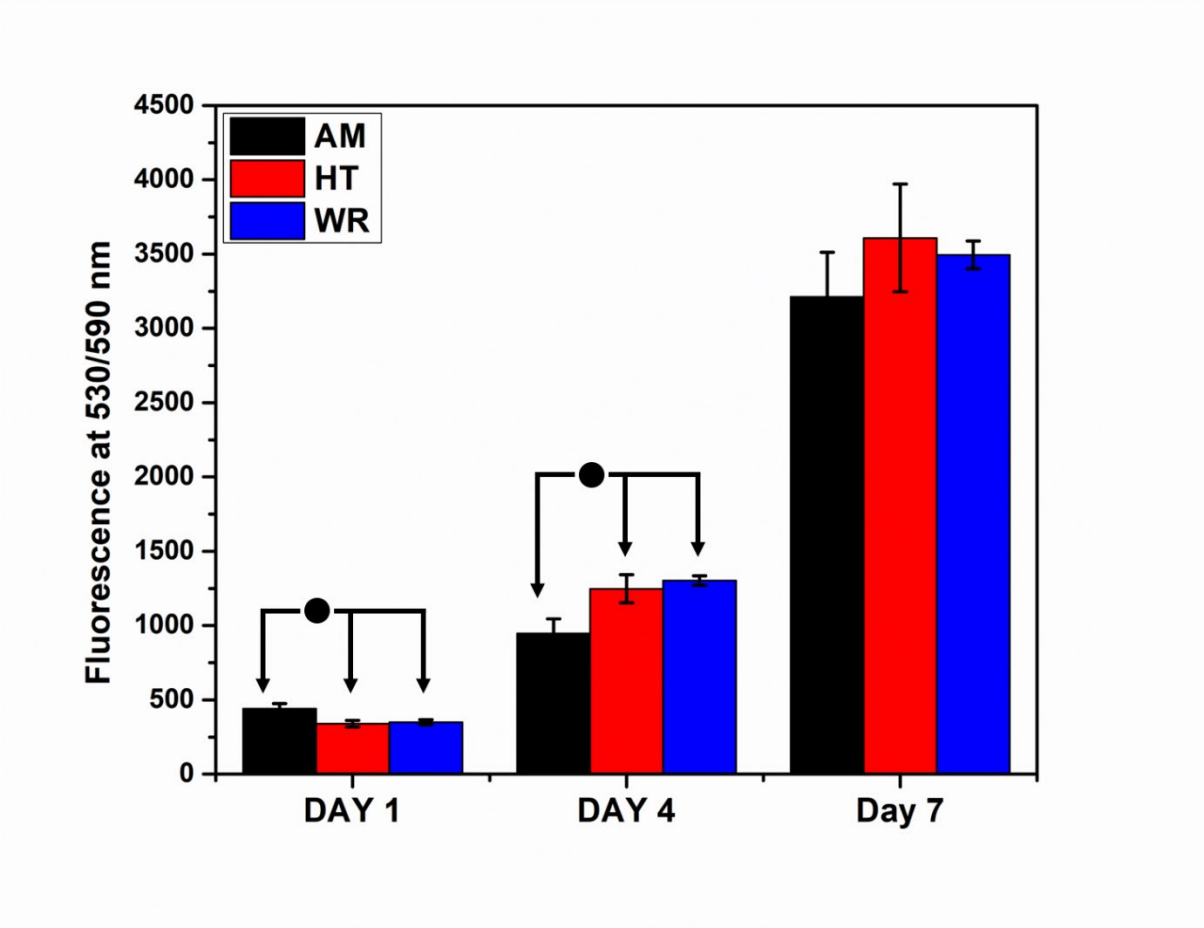

Figure 12 *Fluorescence intensity for Alamar blue assay indicating viability of MC3T3-E1 osteoblasts cultured on AM, HT, and WR.* ● *Indicates statistically significant (p> 0.05) differences. Data are shown as mean ± S.D. for n=3.*

Figure 13

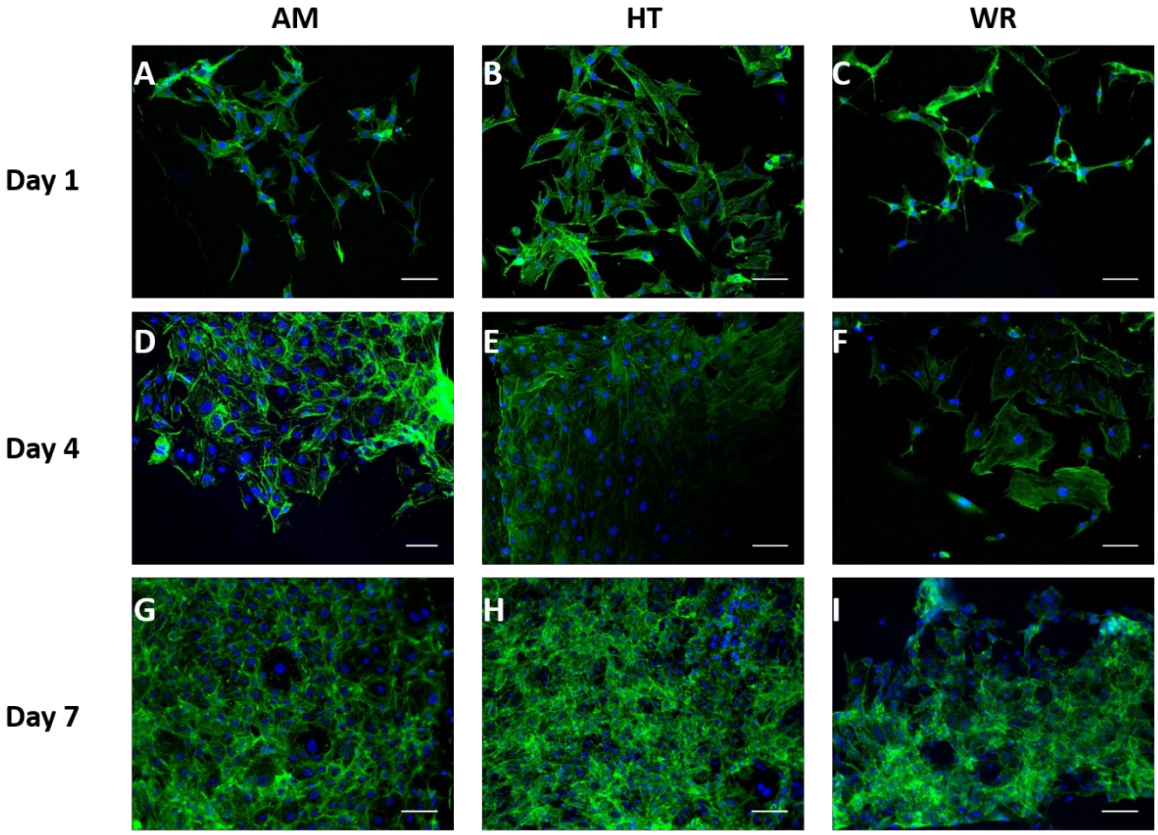

Figure 13 *Fluorescence micrographs of osteoblasts at days 1 4 and 7 on AM, HT and WR surfaces. Blue and green colors represent the nuclei and actin filaments, respectively. Scale bar is 100 μm*

Figure 14

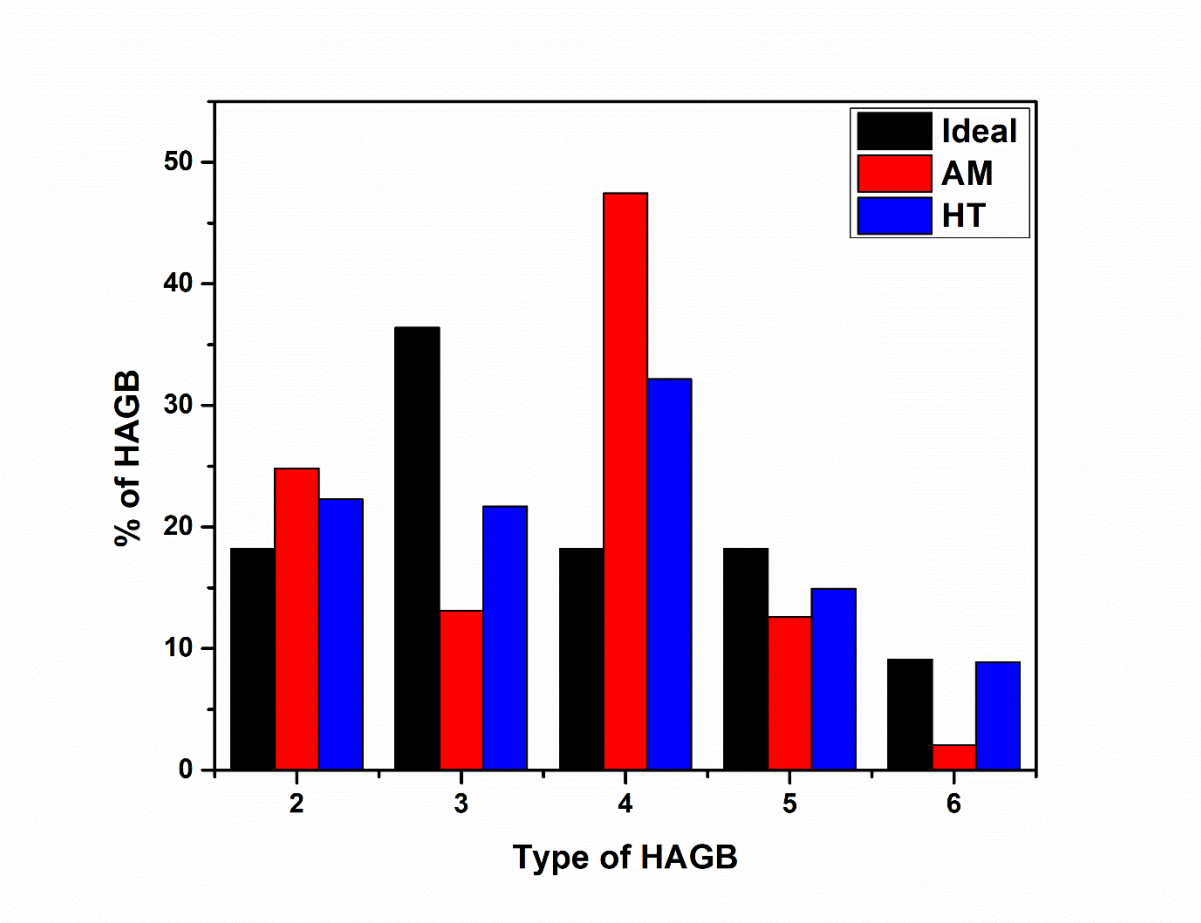

Figure 14 *Plot showing variation of ratio between HAGBs*

Supporting Information for

Enhanced Biomechanical Performance of Additively Manufactured Ti-6Al-4V Bone Plates

Saurabh Kumar Gupta[1], Nagur Shahidsha[1], Sumit Bahl[1,#], Dhaval Kedaria[1], Sarat Singamneni[2], Prasad K.D.V. Yarlagadda[3], Satyam Suwas[1], Kaushik Chatterjee[1*]

[1]Department of Materials Engineering, Indian Institute of Science, Bangalore, India

[2]Department of Mechanical Engineering, Auckland University of Technology, Auckland, New Zealand

[3]School of Chemistry, Physics and Mechanical Engineering, Science and Engineering Faculty, Queensland University of Technology, Brisbane, Australia

*****Author to whom all correspondence should be addressed:*

kchatterjee@iisc.ac.in; +91-80-22933408

[#]Current address: Oak Ridge National Laboratory, Oak Ridge, TN, USA

Table S1 *FWHM (°) of the peaks for AM, HT and WR plate*

Peak	**AM**	**HT**	**WR**
$10\bar{1}0$	0.27	0.15	0.20
0002	0.23	0.13	0.17
$10\bar{1}1$	0.27	0.14	0.19
$10\bar{1}2$	0.30	0.15	0.18
$11\bar{2}0$	0.45	0.24	0.26
$10\bar{1}3$	0.44	0.21	0.20

Figure S1

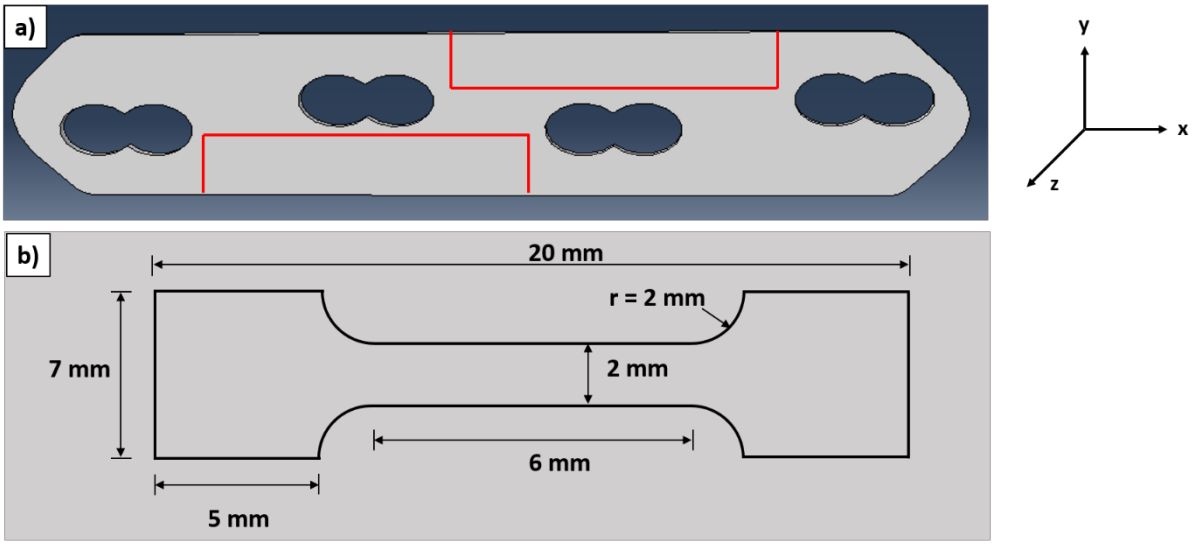

Figure S1 *(a) Top view of the bone plate showing regions for making tensile specimens (XY as gauge region) (b) Dimensions for micro tensile specimen*

Figure S2

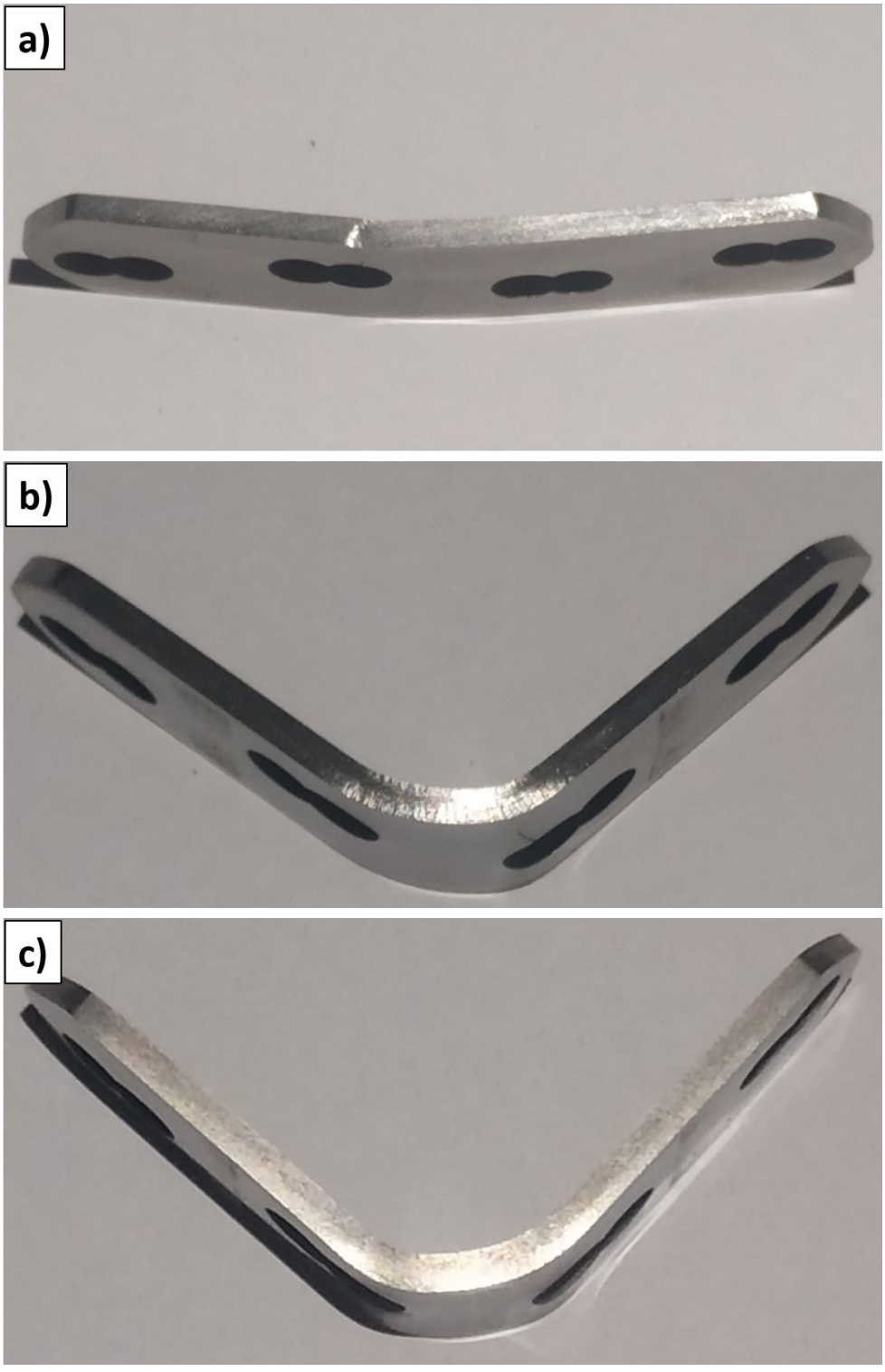

Figure S2 *Images of (a) AM, (b) HT and (c) WR plates after the 3-point bend tests just at the onset of crack formation*

Figure S3

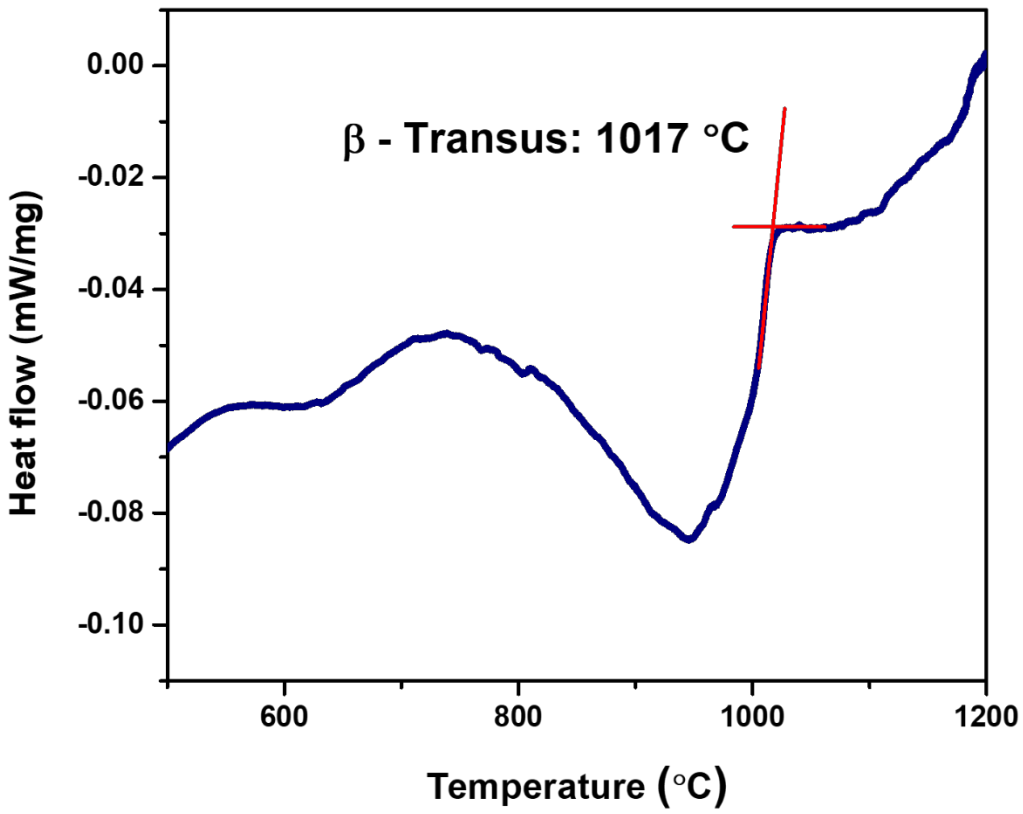

Figure S3 *DSC curve showing β-transus temperature of AM alloy*